Biophysical Journal
Article

Biophysical Society

EB3-informed dynamics of the microtubule stabilizing cap during stalled growth

Maurits Kok,[1] Florian Huber,[1,2,3] Svenja-Marei Kalisch,[1] and Marileen Dogterom[1,*]
[1]Department of Bionanoscience, Kavli Institute of Nanoscience, Faculty of Applied Sciences, Delft University of Technology, Delft, the Netherlands; [2]Netherlands eScience Center, Amsterdam, the Netherlands; and [3]Center for Digitalisation and Digitality, Düsseldorf University of Applied Sciences, Düsseldorf, Germany

ABSTRACT Microtubule stability is known to be governed by a stabilizing GTP/GDP-Pi cap, but the exact relation between growth velocity, GTP hydrolysis, and catastrophes remains unclear. We investigate the dynamics of the stabilizing cap through in vitro reconstitution of microtubule dynamics in contact with microfabricated barriers, using the plus-end binding protein GFP-EB3 as a marker for the nucleotide state of the tip. The interaction of growing microtubules with steric objects is known to slow down microtubule growth and accelerate catastrophes. We show that the lifetime distributions of stalled microtubules, as well as the corresponding lifetime distributions of freely growing microtubules, can be fully described with a simple phenomenological 1D model based on noisy microtubule growth and a single EB3-dependent hydrolysis rate. This same model is furthermore capable of explaining both the previously reported mild catastrophe dependence on microtubule growth rates and the catastrophe statistics during tubulin washout experiments.

SIGNIFICANCE Microtubules are cytoskeletal filaments that exhibit dynamic instability, characterized by random transitions between growing and shrinking states. The transition from growth to shrinking is called a catastrophe and this transition is known to result from the loss of a stabilizing cap due to the hydrolysis of the GTP nucleotide that is associated with tubulin dimers as microtubules grow. To better understand the relation between GTP cap dynamics and the rate at which catastrophes occur, we study the statistics of catastrophe events for microtubules that are stalled by microfabricated barriers using a fluorescent marker to visualize the GTP cap. We introduce a simple one-dimensional model to explain our data as well as previous experimental results on microtubule catastrophes.

INTRODUCTION

Microtubules are hollow cylindrical polymers consisting of αβ tubulin dimers arranged in a head-to-tail fashion to form protofilaments, ∼13 of which typically constitute the microtubule lattice (1–3). Individual microtubules constantly switch between phases of growth and shrinkage, a fundamental process known as dynamic instability (4). As a major constituent of the eukaryotic cytoskeleton, microtubules are involved in many essential processes within the cell, including intracellular transport, cell division, and cell morphology (5). During these processes, dynamic microtubule ends interact with other cellular components, either through intermediary protein complexes or through direct physical contact (6–11). Such contacts typically affect the dynamic behavior of microtubule ends, which is integral to the biological function of these interactions (12–18).

The biochemical mechanism behind the stochastic transition from growth to shrinkage, known as a catastrophe, is related to the progressive hydrolysis of GTP bound to β tubulin (19,20). During polymerization, the microtubule tip is highly dynamic due to continuous addition and removal of tubulin dimers (21–25). After GTP-bound tubulin is incorporated at the microtubule tip, hydrolysis of the nucleotide followed by Pi release is hypothesized to lead to a destabilization of the lattice by a compaction around the exchangeable nucleotide (1,26). The delay between tubulin incorporation and hydrolysis results in a GTP/GDP-Pi-enriched region at the microtubule tip, which gives rise to what is known as the stabilizing cap (27). Upon the loss of the stabilizing cap, a catastrophe follows upon which the strain build-up in the lattice is released during depolymerization. However, whereas this basic description of the biochemistry behind dynamic instability is generally

Submitted June 7, 2024, and accepted for publication November 25, 2024.
*Correspondence: m.dogterom@tudelft.nl
Editor: Kristen Verhey.
https://doi.org/10.1016/j.bpj.2024.11.3314

accepted, the exact relation between GTP hydrolysis, the size of the stabilizing cap, the details of microtubule growth, and the statistics of catastrophes is still not fully understood, despite the availability of a wealth of quantitative data on catastrophe statistics under different conditions (28–31).

Various estimates of the stabilizing cap size have been reported, from short caps of a few terminal tubulin layers (32–37) to longer caps spanning up to dozens of layers (27,38). In recent years, direct visualization of the tubulin nucleotide state has become possible with the family of end binding proteins (EBs) that can autonomously bind to the GTP/GDP-Pi region at the microtubule tip (39,40). It has been shown that the size of the EB comet at the tip correlates with the size of the stabilizing cap and consequently with microtubule stability (1,38,40,41). Interestingly, tubulin washout experiments using Mal3 (the EB1 homolog in yeast) suggest that it is not the size of the total EB binding region that is decisive in preventing a catastrophe, but the presence of a critical number of unhydrolyzed subunits at the terminal ∼10 tubulin layers at the microtubule tip (∼130 dimers) (41).

Here, we use the ability of EB3 to report on the status of the stabilizing cap to investigate the detailed relation between cap dynamics and catastrophe statistics for stalling microtubules that are pushing against microfabricated barriers. A stalling microtubule exerts a pushing force that is too small to overcome its critical buckling force, resulting in the blocking of further microtubule growth. The stability of pushing microtubules has been studied previously for buckling and bending microtubules in vitro (42), in vivo (43–45), and in silico (46,47). It was established that microtubules generating pushing forces against rigid barriers in vitro experience an increased catastrophe frequency (42,48). This force-induced catastrophe is thought to be the result of a reduction in the addition of tubulin dimers as the microtubule growth velocity is slowed with increasing force (22,42). However, exactly how the reduction of tubulin addition in combination with nucleotide hydrolysis affects the dynamics of the stabilizing cap, and thereby determines the lifetime statistics for stalled microtubules, has remained unresolved.

We determine the lifetime statistics of stalling microtubules in vitro by growing microtubules against microfabricated barriers using GFP-EB3 as a proxy for the size of the stabilizing cap. By introducing a novel barrier design with a long overhang, we ensure that microtubule stalling can be imaged simultaneously with the EB3 signal using total internal reflection fluorescence (TIRF) microscopy. We observe that microtubule stalling increases the catastrophe frequency in the absence of EB3 as reported previously (42). In the presence of EB3, the microtubule lifetime is further reduced in a concentration-dependent manner. Surprisingly, the full decay of the EB3 comet during microtubule stalling does not necessarily lead to an immediate catastrophe. We compare our results with similar data obtained for freely growing microtubules under the same conditions, and then perform simulations of microtubule dynamics based on a simple model in an attempt to simultaneously explain both data sets.

Over the years, different types of models have been proposed to gain a better understanding of what triggers a catastrophe. Biochemical models rely on the hydrolysis of tubulin dimers to reduce the size of the stabilizing cap to trigger a catastrophe (21,35,49–54). However, only with the introduction of lateral interactions between dimers in a two-dimensional (2D) model can these models capture observed growth fluctuations (21) and observed microtubule lifetimes (55,56). Mechanochemical models additionally include the build-up of strain in the lattice and protofilament bending at the tip (57–63). Both types of models can explain a variety of experimental observations of dynamic instability, but they typically require many fitting parameters and do not explicitly include the highly dynamic nature of the microtubule tip. Alternatively, simple phenomenological models have been useful in obtaining an intuitive insight into the principles behind microtubule dynamics and the effect of microtubule-associated proteins (24,35,41,64).

To find a minimal model capable of explaining microtubule catastrophe statistics with the smallest possible number of fitting parameters, we use coarse-grained Monte Carlo simulations of 1D filaments (24,52,64,65). We show that the lifetimes of both freely growing and stalled microtubules can be explained by a combination of random GTP hydrolysis and a parameter that characterizes the noisiness of microtubule growth, a concept that was generally missing from previous phenomenological models in the description of microtubule lifetimes. These simulations do not take into account the large amount of available information on how real 3D microtubules grow (30,31,66,67), but rather consider a single parameter characterizing the effective noisiness of microtubule growth that may result from specific 3D molecular mechanisms. We confirm that, while the EB binding region is a measure for the size of the stabilizing cap, there is no one-to-one correlation between its presence and the onset of a catastrophe. Instead, the data are consistent with a catastrophe being triggered when a large enough uninterrupted sequence of GDP-bound tubulin dimers becomes exposed at the microtubule tip, consistent with the idea that only the presence of a critical number of unhydrolyzed subunits near the microtubule tip prevents catastrophes from happening (41). Importantly, this 1D biochemical model can also successfully capture the previously reported catastrophe dependence on tubulin concentration, taking into account previously reported velocity-dependent growth fluctuations, and it is in good agreement with previously reported catastrophe delays after tubulin dilution. The so-called aging of microtubules, referring to the observed increase of the catastrophe frequency with microtubule age (58,68–70), is not an intrinsic feature of our simple model, but this behavior naturally emerges by

additionally assuming that microtubule growth fluctuations increase with microtubule age.

MATERIALS AND METHODS

Proteins

GFP-EB3 was a kind gift from Michel Steinmetz. All tubulin products were acquired from Cytoskeleton, Denver, Colorado, USA, with all unlabeled tubulin specifically from a single lot.

Microfabrication of barriers

The fabrication method for the microfabricated barriers with an SiC overhang is inspired by (71), (72), and (73). All fabrication steps were performed in a cleanroom environment (van Leeuwenhoek Laboratory, NanoLab NL). The barrier was designed with the following considerations in mind.

1) The width of the channels should favor stalling events over buckling events, but remain large enough for GMPCPP-stabilized seeds to easily land.
2) A bottom layer of SiC is needed to prevent etching into the coverslip during a buffered oxide etch. This layer needs to be as thin as possible to prevent photon absorption by the semiconductor resulting in a diminished signal/noise and surface heating. Although SiC is transparent for wavelengths >0.5 μm, its bandgap of ∼2.8 eV can result in photon absorption for the commonly used 405 and 488 nm lasers (74). Using plasma-enhanced chemical vapor deposition (PE-CVD), 10 nm is the thinnest layer we could fabricate while still maintaining the layer's integrity to protect the coverslip from the buffered oxide etch.
3) The layer of SiO_2 of 100 nm ensures that the microtubule can polymerize underneath the overhang while remaining inside the evanescent wave.
4) The top layer of SiC is 250 nm thick to ensure mechanical stability, while still allowing to observe microtubules growing on top of the barrier despite some photon absorption.

To start, glass coverslips (24 × 24 mm, no. 1) were cleaned for 10 min with base piranha, a mixture of H_2O:NH_4OH:H_2O_2 in a 5:1:1 ratio heated to 70°C. Then, three sequential layers of SiC (10 nm), SiO_2 (100 nm), and SiC (250 nm) are deposited on the cleaned surface via PE-CVD at 300°C (Oxford Instruments PlasmaPro 80, Abingdon, Oxfordshire, UK). PE-CVD ensures a surface smooth enough for TIRF microscopy with fast deposition rates (70 nm/min for SiO_2 and 40 nm/min for SiC).

To transfer the barrier pattern to the surface, UV lithography is used. First, to aid in the adhesion of the photoresist, a few drops of hexamethyldisilazane are spin coated on the SiC surface and allowed to dry on a 115°C hotplate for 30 s. Then a 1.3 μm layer of the positive photoresist S1813 (MicroChem, Westborough, Massachusetts, USA) is spin coated (5000 rpm) on the surface and prebaked for 90 s on a 115°C hotplate. Exposure of the photoresist through a chromium mask with a near-UV source (320–365 nm, ∼13 mW/cm^2) transfers the barrier pattern in 4 s (EVgroup EVG 620, St. Florian am Inn, Austria). Development with MF321 (MicroPosit [Shipley Company]—acquired by Dow) for 60 s removes the UV-exposed regions of the resist.

Next, reactive ion etching (Leybold GmbH, Cologne, Germany; Heraeus Group, Hanau, Germany) with a mixture of CHF_3:O_2 (50:2.5 sccm) etches through the exposed regions of the 250 nm SiC layer and into the SiO_2 layer. The etch is performed at 50 μbar and at 100 W, resulting in a bias voltage of 400 V. It is important to etch completely through the top SiC layer, but only partly through the SiO_2 layer, to leave the bottom SiC layer intact. Any remaining photoresist after the etch is removed by sonication of the sample in acetone for 10 min.

Finally, the sample is submerged in buffered hydrofluoric acid (HF:NH_4F = 12.5:87.5%) to selectively etch the exposed SiO_2 with a rate of approximately 200 nm/min to obtain an overhang of 1.5 μm. The final barriers are 100 nm high with an overhang of 1.5 μm, enclosing channels with a width of 15 μm.

In vitro microtubule dynamics assay

Reconstitution of microtubule dynamics was performed as previously described in (75,76). After cleaning the barrier sample with O_2-plasma, a flow channel was constructed with a cleaned glass slide and double-sided sticky tape in such a way that the channel direction is perpendicular to the barriers. Then, the surface was consecutively functionalized with 0.5 mg/mL PLL-PEG-biotin (20%) (SuSoS AG, Duebendorf, Switzerland), 0.2 mg/mL NeutrAvidin (Invitrogen, Waltham, Massachusetts, USA), and 0.5 mg/mL κ-casein (Sigma, St. Louis, Missouri, USA). All components were kept in MRB80 buffer, comprising 80 mM piperazine-N,N′-bis(2-ethanesulfonic acid), 4 mM $MgCl_2$, and 1 mM EGTA (pH 6.8). The reaction mixture contained 15 μM tubulin (7% rhodamine labeled) in the presence of GFP-EB3- or Hilyte488-labeled tubulin in the absence of GFP-EB3, supplemented with 0.5 mg/mL κ-casein, 0.15% methylcellulose, 50 mM KCl, 1 mM GTP, oxygen scavenger mix (4 mM DTT, 200 μg/mL catalase, 400 μg/mL glucose oxidase, 50 mM glucose). The reaction mix was then centrifuged in an Airfuge (Beckman Coulter, Brea, California, USA) at 30 psi for 8 min to remove any aggregated complexes before being introduced to the sample. GMPCPP-stabilized seeds (70% unlabeled tubulin, 18% biotinylated tubulin, 12% rhodamine-labeled tubulin) were introduced to the channel with the flow direction perpendicular to the barriers. Flow cells were sealed with vacuum grease and imaged on a TIRF microscope at 28–30°C.

TIRF microscopy

All experiments were imaged using TIRF microscopy, consisting of an Ilas^2 system (Roper Scientific, Trenton, New Jersey, USA) on a Nikon Ti-E inverted microscope. The Ilas^2 system is a dual illuminator for azimuthal spinning TIRF illumination equipped with a 150 mW 488 nm laser, a 100 mW 561 nm laser, and a ZT405/488/561/640rpc dichroic mirror. Simultaneous dual-acquisition was performed with two Evolve 512 EMCCD cameras (Photometrics, Tucson, Arizona, USA) through a 525/50 nm and a 609/54 emission filter, using a Nikon CFI Plan Apochromat 100XH NA1.45 TIRF oil objective. Together with an additional magnifying lens, the final magnification resulted in a pixel size of 107 nm/pixel. The sample was heated with a custom objective heater to 28–30°C and was kept in focus with the Nikon Perfect Focus system. The hardware was controlled with MetaMorph 7.8.8.0 (Molecular Devices, San Jose, California, USA).

Image treatment

The image stacks obtained with TIRF microscopy were corrected before data analysis. First, simultaneous acquisition of rhodamine-labeled tubulin and GFP-EB3 on two cameras introduced a nonlinear spatial offset between the two image stacks due to imperfections in the dichroic mirror and in the alignment of the two cameras. By scanning multiple FOVs of a calibration slide containing 100 nm TetraSpeck beads (Thermo Fisher Scientific, Waltham, Massachusetts, USA) and automatically locating the centroids through a custom-written MATLAB script, a nonlinear registration profile accounting for the spatial offset was calculated. The misaligned image stack was corrected by applying this registration profile based on the position of ∼500 bead positions. In addition, any sample drift was corrected by subpixel image registration through cross correlation (77).

Secondly, some scattering of excitation light at the edge of the SiC overhang made proper determination of the GFP-EB3 signal near the barrier difficult. Although this effect was mostly mediated by creating a wide undercut that physically separated the edge of the overhang from the barrier, a correction was nonetheless applied. To correct the signal, the minimum intensity value of each pixel in the image stack was subtracted from that pixel in each image. This correction enabled tracking of the EB3 comet near the barrier and accurate measurement of the EB3 comet intensity.

Thirdly, a general background subtraction was performed in Fiji (78) to correct for inhomogeneous illumination.

Image analysis

Analysis of the images was partly performed with Fiji and with MATLAB. After the image treatment described above, kymographs were created by drawing straight lines of 9-pixel width (0.95 μm) along growing microtubules using the KymoResliceWide plugin with maximum transverse intensity (http://fiji.sc/KymoResliceWide). Each growth event in the kymographs was manually traced to determine the position of the microtubule tip. This position was then used to fit the EB3 comet to obtain its position and intensity, using the intensity profile:

$$I(x) = I_A \cdot exp\left[\frac{(x - x_c)^2}{\sigma^2}\right] + I_{bkg}$$

where $I(x)$ is the fluorescence intensity, I_{bkg} is the background intensity, I_A is the intensity amplitude, x_c is the position of the peak of the EB3 comet, and σ is the width of the EB3 comet. As EB3 comet decay at the barrier makes fitting impossible, the intensity during contact was determined by calculating the average intensity value in a region around the comet position and around the barrier (Fig. S1 *C*). The barrier contact duration and comet decay duration were determined manually.

Monte Carlo simulations

Simulations of growing microtubules were run as a series of discrete, fixed time steps. Microtubules were modeled as simplified 1D structures thereby ignoring their actual 3D helical structure. The length of the time steps δt was chosen small enough to properly account for the random hydrolysis of the subunits (P_{hyd}, the probability for a dimer to undergo hydrolysis within one time step was kept at <0.05). Further restrictions were to not exceed the desired frame rate, in our case the lowest used experimental frame rate of 250 ms. Due to the discrete nature of microtubule growth in subunits, the next-lowest time step for which $\langle V\rangle\delta t/L_0$ became an integer was chosen, with $L_0 = \frac{8}{13}$ nm the length increment per subunit and $\langle V\rangle$ the microtubule mean growth velocity.

Each microtubule simulation started from a few initial subunits (a "seed") that were excluded from hydrolysis, and that were not allowed to be removed during microtubule tip fluctuations. Microtubule growth was simulated as a discrete, biased, Gaussian random walk. This means that, for each time step δt, the microtubule length was changed by a discretized random number of subunits that was drawn from a Gaussian distribution with standard deviation $\sigma = \sqrt{2D_{tip}\delta t}$ and centered at $\langle dx\rangle/\ L_0$.

During each time step, subunits transition from the GTP/GDP-Pi to the GDP state by random hydrolysis with a rate k_{hyd}. Whenever the foremost uninterrupted strand of GDP state subunits ($\geq N_{unstable}$ subunits in a row) is changed, the position of the end of the stable cap will jump to the front element of this strand, which we interpret as the new position of the end of the stable cap $L_{end-of-cap}$.

A simulation run ends when a catastrophe occurs. This happens when the stable cap shrinks to zero, i.e., if $L_{tip} - L_{end-of-cap} = 0$, where L_{tip} is defined as the position of the foremost subunit of the microtubule. The growth duration was defined as the time from initial growth until catastrophe. To exclude nucleation kinetics from the simulated lifetimes, a microtubule is considered to grow after reaching a length of 250 nm.

The presence of a physical barrier is modeled by introducing a fixed barrier position $L_{barrier}$. Tip dynamics and random hydrolysis remained unchanged, only the microtubule length was truncated whenever it would penetrate the barrier. This means the length of the microtubule was set back to $L_{barrier}$ if $L_{tip} > L_{barrier}$. The barrier contact time was then defined as the time from the microtubules' first contact with the barrier until its catastrophe.

The simulation was written in Python and run on standard PCs. The code to run the simulation is available under an open license on GitHub (https://github.com/florian-huber/mtdynamics).

Analytical expression for the size of the stabilizing cap

The length of the stabilizing cap L_{cap} is defined as the distance between the position of the microtubule tip and the first occurrence of a sequence of hydrolyzed subunits N equal or greater than $N_{unstable}$. The location of this sequence of hydrolyzed subunits is determined by the distribution of GDP dimers in the microtubule lattice. We assume that the GTP/GDP-Pi distribution at the microtubule tip decays monoexponentially and depends on the hydrolysis rate k_{hyd} and mean growth velocity $\langle V\rangle$ (38,41,76). The probability $p(x)$ of finding a GTP/GDP-Pi subunit at position x in the lattice (with the microtubule tip at $x = 0$) corresponds to

$$p(x) = e^{-x\frac{k_{hyd}}{\langle V\rangle}} \tag{1a}$$

with the probability of finding a GDP subunit at position x being

$$q(x) = 1 - p(x) \tag{1b}$$

To find the probability distribution of the position of a sequence of N sequential hydrolyzed dimers equal to or greater than $N_{unstable}$, we treat the discrete 1D lattice as a series of independent Bernoulli trials with probabilities $p(x)$ and $q(x)$ for GTP/GDP-Pi or GDP dimers, respectively (Fig. S5 *A*). For a lattice shorter than N, the probability of finding a sequence of N GDP is zero since the sequence is longer than the considered lattice. The probability of finding N GDP subunits between the positions $x = 1$ and $x = N$ is equal to the product of the probability at each position x:

$$P_{GDP} = \prod_{x=1}^{N} q(x) \tag{2a}$$

If N and $\frac{k_{hyd}}{\langle V\rangle}$ are small, the probability of finding a GDP subunit at the beginning of the sequence is approximately equal to that at the end, i.e., $q(x_1) \approx q(x_N)$. Using this assumption, Eq. 2a can be rewritten as

$$P_{GDP} = q(x)^N \tag{2b}$$

For a position on the lattice further from the tip, the probability of finding a sequence $N \geq N_{unstable}$ at position x, with x being the first position of the sequence, is equal to

$$P_{GDP}(x) = p(x)q(x)^N \tag{3}$$

as the dimer directly preceding the sequence needs to be unhydrolyzed to initiate the sequence (Fig. S5 *A*).

We can now obtain an expression for the probability of finding this sequence for *the first time* at position x, by considering the probability that no sequence is found at any position closer to the microtubule tip:

$$P(x|N) = 1 - \prod_{i=1}^{x-1}\left[1 - p(x_i)q(x_i)^N\right] \tag{4}$$

This expression gives the cumulative distribution for finding a sequence of N GDP subunits at position x during steady-state growth. We find that this approximation holds reasonably well for the entire range of $N_{unstable}$ we explored using the 1D simulation (Fig. S5 *B*). The probability of finding

this sequence of GDP can be captured by the Gaussian cumulative distribution function:

$$P_{cap}(x) = \frac{1}{2}\left[1 + \mathrm{erf}\left(\frac{(x - L_{cap})}{\sqrt{2}\sigma_{cap}}\right)\right] \quad (5)$$

Through numerical analysis we find that the dependency of L_{cap} on N follows a power law and can be described with

$$L_{cap}(N) = \alpha\left(N^{\beta} - 1\right),$$

where α and β are coefficients that depend on the hydrolysis rate and the growth velocity. Similarly, we can calculate the dependence of the cap size on the parameters k_{hyd} and $\langle V\rangle$.

Analytical expression for the catastrophe probability and microtubule lifetimes

The probability for a microtubule to undergo a catastrophe within time window Δt is defined as $P_{cat}(\Delta t)$ and is equal to the probability of reducing the cap size L_{cap} to zero during Δt. The cap size evolves by two competing stochastic processes: it increases by dimer addition at the tip and shrinks by dimer removal from the tip and hydrolysis in the lattice. To obtain an analytical expression for the catastrophe probability, we consider a microtubule at steady-state growth. In this frame of reference, the end of the cap is on average a constant distance from the microtubule tip, as both the microtubule tip and the position of the cap end move with equal velocity $\langle V\rangle$. Any fluctuations of the cap size during steady-state growth are caused by fluctuations of the tip position. However, due to the stochastic nature of hydrolysis, any incorporated dimers at the microtubule tip position only affect the position of the cap end after a characteristic time delay τ_c, which is approximately equal to ${k_{hyd}}^{-1}$ (Fig. S5 *C*). In other words, the delay gives a measure of the time window during which the fluctuations can affect L_{cap}, before the position of the cap is affected by hydrolysis. The catastrophe probability is then equal to the probability of tip fluctuations exceeding the position of L_{cap} during time window τ_c.

The growth fluctuations at the microtubule tip can be described by a biased random walk with Gaussian distributed steps Δx within Δt.

$$P_{tip}(\Delta x, \Delta t) = \frac{1}{\sqrt{4\pi D_{tip}\Delta t}}\exp\left(-\frac{(\Delta x - \langle V\rangle\Delta t)^2}{4D_{tip}\Delta t}\right) \quad (6)$$

Note that, in the frame of reference of steady-state growth, $\langle V\rangle = 0$. To find $P_{cat}(\Delta t)$, we calculate the probability that the microtubule tip exceeds L_{cap} during $\Delta t \le \tau_c$. The survival probability, the probability that the microtubule tip does not exceed L_{cap} for all times up to τ_c, is defined as

$$S(x_c|\tau_c) \equiv \mathrm{erf}\left(\frac{x_c - x_0}{\sqrt{4\,D_{tip}\tau_c}}\right) \quad (7a)$$

with x_c being the critical cap-end position. Since the critical cap-end position is defined with respect to x_0 being the moving tip, we can set $x_0 = 0$ and get the probability for the tip to have reached $x \ge x_c$:

$$P_{tip}(x \ge x_c|\tau_c) = 1 - S(x_c|\tau_c) = 1 - \mathrm{erf}\left(\frac{x_c}{\sqrt{4\,D_{tip}\tau_c}}\right) \quad (7b)$$

When we set $x_c = L_{cap}$, we can calculate the catastrophe probability $P_{cat}(\tau_c)$ as the probability of the tip fluctuations exceeding the cap size L_{cap} during time window τ_c with

$$P_{cat}(\tau_c) = P_{tip}\left(x \ge L_{cap}|\tau_c\right) = 1 - \mathrm{erf}\left(\frac{L_{cap}}{\sqrt{4\,D_{tip}\tau_c}}\right) \quad (8)$$

The microtubule lifetime distribution $T_{cat}(t)$ can then be obtained by calculating the fraction of microtubules that underwent a catastrophe after each time step τ_c:

$$T_{cat}(t) = 1 - (1 - P_{cat}(\tau_c))^{\frac{t}{\tau_c}} \quad (9)$$

Note that the steady-state approximation becomes less accurate for large $\frac{k_{hyd}}{\langle V\rangle}$ as steady-state growth might not be reached in the first place. This leads to a lack of short events and consequently to an overestimation of the microtubule lifetimes.

RESULTS

In vitro reconstitution of microtubule stalling

To investigate the stability of stalling microtubules in the presence of different concentrations of GFP-EB3, we analyzed the dynamics of microtubules growing against microfabricated barriers using an in vitro reconstitution assay (71,76). We assume each microtubule to consist of three regions: 1) a terminal region where net microtubule growth takes place by addition and removal of tubulin dimers (60,79), 2) a GTP/GDP-Pi region near the microtubule tip to which EB3 preferably binds leading to the appearance of EB3 comets (39,40), and 3) the GDP lattice (Fig. 1 *A*). Note that recent experiments suggest that EB3 binds preferentially to the GTP state rather than the GDP-Pi state (40), but for the sake of simplicity we do not distinguish between these two nucleotide states. The presence of EB3 is known to increase both the GTP hydrolysis rate and the microtubule growth velocity by respectively compacting the microtubule lattice and closing the lattice seam (1,79). Microtubules were nucleated from GMPCPP-stabilized seeds and imaged with TIRF microscopy. The barriers were composed of 100 nm SiO_2 deposited on a glass coverslip with an amorphous silicon carbide (SiC) overhang, approximately 1.5 μm long, to trap the microtubules and force them to grow into the barriers (Fig. 1, *B* and *C*). SiC is a mechanically stable, optically transparent material (wavelengths >0.5 μm) with similar passivation and functionalization properties as SiO_2 due to a very thin native oxide layer on its surface (80,81). Although fabrication of the barriers requires a thin 10 nm layer of SiC on the glass surface (see materials and methods for details), microtubules can be imaged successfully with TIRF microscopy (Figs. 1 *D* and S1). This novel barrier design enables high-resolution imaging with TIRF microscopy as the microtubules are forced to remain within 100 nm from the surface during barrier contact, eliminating fluctuations perpendicular

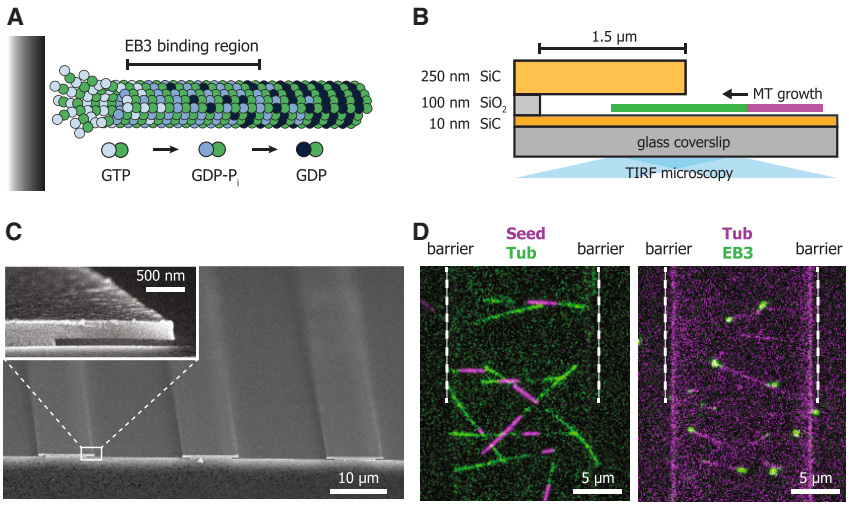

FIGURE 1 In vitro reconstitution of microtubule stalling. (*A*) Schematic depiction of the nucleotide distribution at the microtubule tip. Progressive hydrolysis of GTP-tubulin after incorporation leads to a destabilized lattice that is stabilized by a GTP/GDP-Pi cap. EB3 chiefly binds to the GTP/GDP-Pi-rich region. During microtubule-barrier contact, reduction of microtubule growth and ongoing hydrolysis are hypothesized to lead to an accelerated loss of the protective cap. (*B*) Schematic of the microfabricated barrier with a 1.5 μm overhang made of silicon carbide (SiC). The barrier itself is composed of SiO_2 and is 100 nm high, forcing the growing microtubules to remain within the TIRF illumination field. Microtubules are grown from stabilized GMPCPP seeds. (*C*) Scanning electron microscope image of two channels with barriers. The inset shows a zoom of the barrier with a 1.5 μm SiC overhang. (*D*) TIRF images of the microfabricated channel enclosed by two barriers (*white dotted lines*). On the left, microtubules (*green*) are nucleated from GMPCPP-stabilized seeds (*magenta*) toward the barriers, and on the right, microtubules (*magenta*) polymerize toward the barriers in the presence of GFP-EB3 (*green*). See also Fig. S1 and Videos S1 and S2.

to the surface. The width between two barriers is 15 μm, chosen to keep the microtubules short and thereby reduce the probability of observing slipping and buckling events (42). All experiments were performed in the presence of 15 μM tubulin, and 0, 20, 50, or 100 nM GFP-EB3.

Complete EB3 decay is neither needed for, nor always immediately followed by a catastrophe

The microtubule-barrier contact events leading to a stalling microtubule were analyzed with kymographs to obtain the contact duration and GFP-EB3 comet intensity before and during contact (Figs. 2 *A* and S1, see materials and methods for details). Any contact events leading to microtubule buckling or sliding along the barrier were excluded from the analysis. From the moment of barrier contact, the EB3 intensity at the microtubule tip decreased until the onset of catastrophe (Figs. 2 *B* and S1 *D*). We observed that, for ~65% of all stalling events, a catastrophe occurred while the EB comet was still decaying (>10% of the EB signal remaining) (Fig. 2 *C*, *right*). For those events, the mean comet intensity at the moment of catastrophe was 16% of the pre-contact mean. For the remaining ~35% of stalling events we found a decay of the EB comet to a steady near-zero value, which did not immediately lead to catastrophe. Instead, the microtubules remained in contact with the barrier for some time, even in the absence of an observable EB3 comet (Fig. 2 *C*, *left*). Fitting the average EB decay from the moment of barrier contact with a monoexponential function shows that the decay rate increases with EB3 concentration: 0.24 ± 0.01, 0.29 ± 0.01, and 0.40 ± 0.04 s^{-1} (95% CI) for 20, 50, and 100 nM EB3, respectively (Fig. 2 *D*). The presence of EB3 thus accelerates the decay of the EB comet during stalling events as predicted from its increasing effect on the GTP hydrolysis rate (1,79).

Monte Carlo simulation of microtubule catastrophes

To determine whether microtubule lifetime statistics of stalling microtubules can be understood solely by a single stochastic hydrolysis step combined with net stalling of noisy microtubule growth, we performed minimalistic Monte Carlo simulations of both free and stalled microtubule growth. Microtubules were treated as 1D filaments with subunits of 8/13 nm comprising two distinct states: GTP/GDP-Pi and GDP (Fig. 3 *A*). We decided to ignore the initial transition from GTP to GDP-Pi, which was reported to be much faster than the GDP-Pi to GDP transition (24,79,82). We saw this justified by the fact that our key observations changed only very moderately when the first transition was included explicitly, whereas omitting this transition reduced the number of model parameters. Simulated microtubules grow by addition of GTP/GDP-Pi subunits which subsequently undergo random hydrolysis to GDP with rate k_{hyd} (Fig. 3 *A*). We treat microtubule growth as a discrete, biased Gaussian random walk (64,83), inspired by experimental observations that revealed a substantial diffusive character of the growing microtubule tip (21–24). Following this model, tip growth is fully characterized by the experimentally measured mean growth velocity $\langle V \rangle$ and the diffusion constant D_{tip}, which may also result in occasional negative growth excursions (Fig. 3 *B*). A catastrophe is triggered when a stabilizing cap (L_{cap}) that results from remaining GTP/GDP-Pi subunits is lost due to a negative growth excursion and/or random hydrolysis. We assume that the nucleotide state of the tubulins at the very tip of the microtubule are the most relevant for stability: a catastrophe is triggered when the number of uninterrupted GDP subunits in a sequence at the very tip of the microtubule is equal to or greater than $N_{unstable}$ (35,52), independent of how many GTP/GDP-Pi subunits remain elsewhere in the lattice

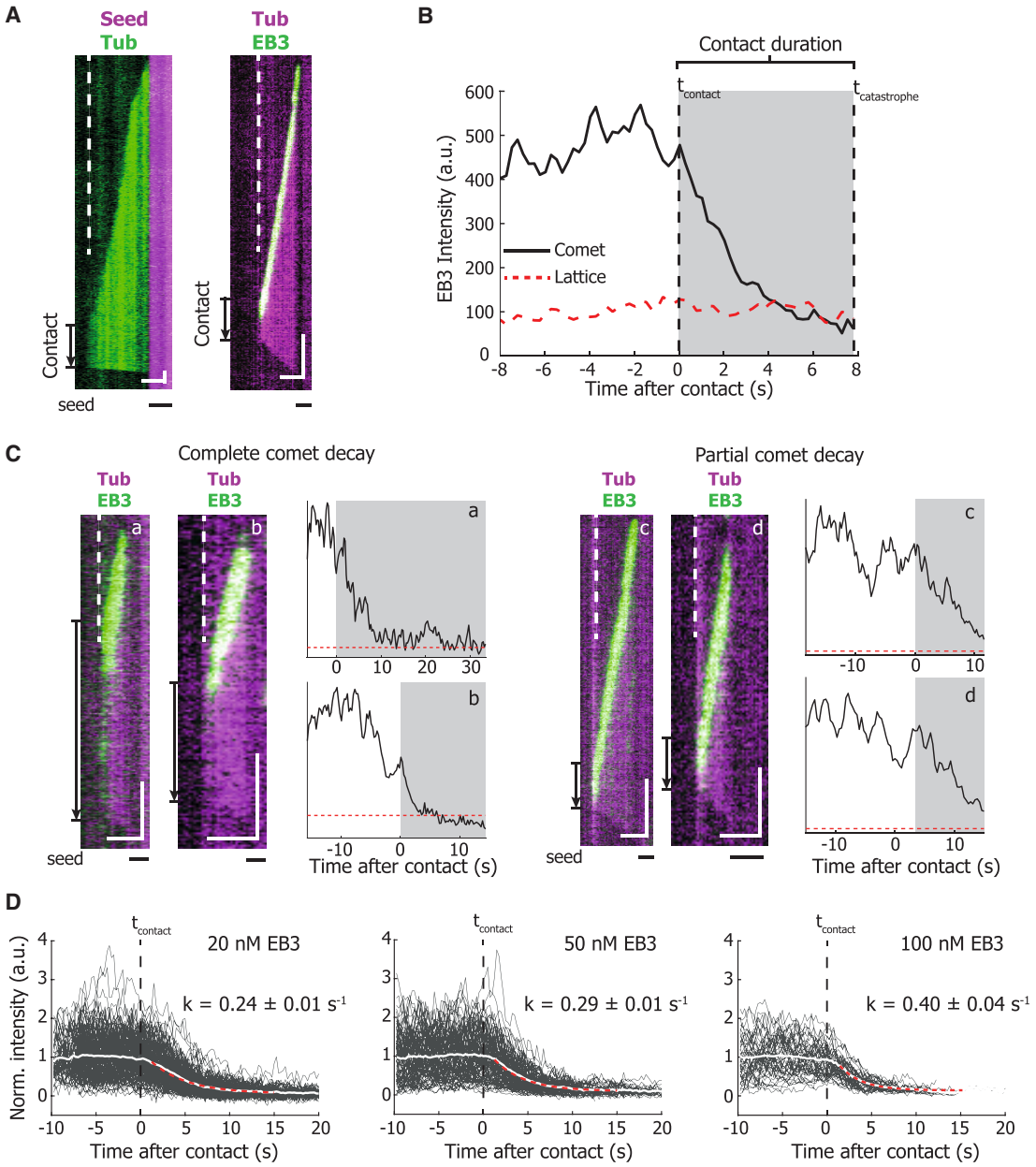

FIGURE 2 Microtubule stalling events in vitro. (*A*) Representative kymographs of a microtubule-barrier contact event in the presence of 15 μM Hilyte488-labeled tubulin (*left*) and in the presence of 15 μM rhodamine-labeled tubulin with 20 nM GFP-EB3 (*right*). The dotted line denotes the position of the SiO_2 barrier. The duration of barrier contact is indicated with an arrow. Scale bars, 2 μm (*horizontal*) and 10 s (*vertical*). (*B*) Mean intensity of the EB3 comet and the EB3 signal on the microtubule lattice of the kymograph on the right in (*A*). From the moment of microtubule-barrier contact ($t_{contact}$), the EB3 comet signal decays to the level of the microtubule lattice, ultimately resulting in the onset of a catastrophe ($t_{catastrophe}$) after 7.75 s. (*C*) Several examples of stalling microtubules with their respective comet intensity traces. Traces a and b show a full comet decay during barrier contact before the onset of a catastrophe, whereas the comet in traces c and d only partially decays. All traces were in the presence of 15 μM tubulin. In addition, trace a contained 20 nM EB3, traces b and c 100 nM EB3, and trace d 50 nM EB3. Arrows and shaded regions illustrate the duration of microtubule stalling event. Scale bars, 2 μm (*horizontal*) and 10 s (*vertical*). (*D*) Normalized comet intensity traces of stalling microtubules in the presence of 20, 50, and 100 nM EB3, aligned on the moment of barrier contact ($t_{contact}$). The mean decays were fitted with a monoexponential model (*red dotted line*) and show an increasing decay rate with increasing EB3 concentrations, resulting in decay rates of 0.24 $\pm$ 0.01, 0.29 $\pm$ 0.01, and 0.40 $\pm$ 0.04 s^{-1} (95% CI) for 20, 50, and 100 nM, respectively. Number of stalling events analyzed: 20 nM, $n = 151$, 50 nM, $n = 104$, and 100 nM, $n = 92$.

(Fig. 3 *C*). The length of the stabilizing cap is thus determined by the distance between the position of the microtubule tip and the position along the lattice where for the first time an uninterrupted sequence (or "island") of GDP units equal to or greater than the fitting parameter $N_{unstable}$ is found (Fig. 3 *C*). Depolymerization and rescues are not considered in the model. To exclude nucleation kinetics from the simulated lifetimes, a microtubule is considered

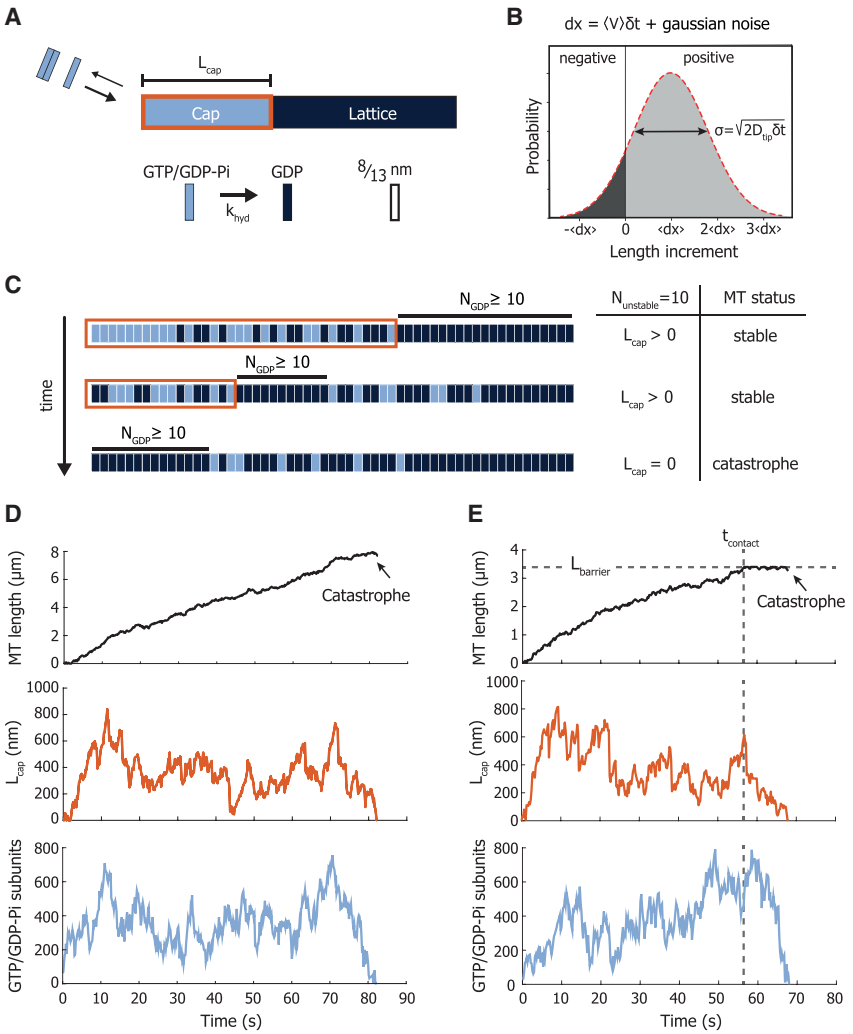

FIGURE 3 Monte Carlo simulation of microtubule dynamics. (*A*) The microtubule is simulated as a one-dimensional lattice with two regions, a cap region with length L_{cap} with predominantly GTP/GDP-Pi subunits and a lattice region with predominantly GDP subunits. The size of each subunit is 8/13 nm. Uncoupled stochastic hydrolysis matures the GTP/GDP-Pi state into the GDP state with rate k_{hyd}. (*B*) Microtubule growth is determined by a mean growth velocity $\langle V \rangle$ with added Gaussian noise characterized by D_{tip}, resulting in stochastic tip elongation following a biased random walk. The diffusive character of the tip can also produce negative growth excursions. (*C*) Detailed schematic of the nucleotide composition of the microtubule tip. The size of the stabilizing cap (*orange*) is defined as the region between the microtubule tip and the position along the lattice where for the first time an uninterrupted sequence of GDP subunits is equal or greater than $N_{unstable}$. A catastrophe is triggered when the number of uninterrupted GDP subunits at the very tip of the microtubule is equal or greater than $N_{unstable}$. As an example, the case for $N_{unstable} = 10$ is shown. (*D*) Simulated microtubule growing event. Top: during the noisy microtubule growth, the microtubule length follows a biased random walk. Middle: when the size of the stabilizing cap (L_{cap}) is reduced to zero, i.e., when the number of uninterrupted terminal GDP subunits is equal or greater than $N_{unstable}$, a catastrophe follows, and the simulation is terminated. Bottom: total number of GTP/GDP-Pi subunits in the simulated microtubule. (*E*) Simulated microtubule stalling event. Figures show the simulated microtubule length (*top*), the size of the stabilizing cap (L_{cap}) (*middle*), and the total number of GTP/GDP-Pi subunits in the simulated microtubule (*bottom*). Barrier contact is simulated by restricting the maximum length of the microtubule to $L_{barrier}$. As the microtubule can undergo occasional negative growth excursions due to noisy growth, the microtubule length can still fluctuate during barrier contact.

to grow after reaching a length of 250 nm. The simulation then only requires the three fitting parameters k_{hyd}, D_{tip}, and $N_{unstable}$, all of which can be verified with experimental data (see below). The experimental EB3 intensity at the microtubule tip (see, e.g., Fig. 2) can be compared with the number of GTP/GDP-Pi subunits in the simulated microtubules (Fig. 3, *D* and *E*, *bottom*).

Microtubule stalling is simulated by introducing a fixed maximum length $L_{barrier}$ (Fig. 3 *E*). Any growth excursions that would bring the microtubule length to $L > L_{barrier}$ are truncated to this maximum length. Since tip fluctuations also include occasional negative growth excursions (Fig. 3 *B*), fluctuations of the tip position continue after barrier contact (Fig. 3 *E*).

Obtaining the simulation parameters

Our 1D model relies on three fitting parameters, D_{tip}, k_{hyd}, and $N_{unstable}$. Based on existing literature (79), we expected that adding EB3 would have an effect on the transition from GTP/GDP-Pi to GDP. Since EB3 also affects the microtubule growth velocity, we also expected that growing microtubules may display different growth fluctuations at different EB concentrations. It hence appeared reasonable to keep k_{hyd} and D_{tip} as free fitting parameters, while keeping $N_{unstable}$ as a global fitting parameter that is independent of the presence of EB3. From the kymograph traces, we obtained values for the growth velocity $\langle V \rangle$ of 1.7 ± 0.4, 2.8 ± 0.5, 2.8 ± 0.5, and 3.7 ± 0.7 μm/min (mean ± SD) for 0, 20, 50, and 100 nM EB3, respectively, and a seed-barrier distance $L_{barrier}$ of 3.4 ± 2.5 μm (mean ± SD) from the experimental data.

To find good fitting values, we performed systematic parameter scans across a range of D_{tip} and k_{hyd}, simulating 500 microtubule growth events for each parameter combination. We simulated both freely growing and stalling microtubules and compared the distributions with the respective experimental distributions. Using a Kolmogorov-Smirnov

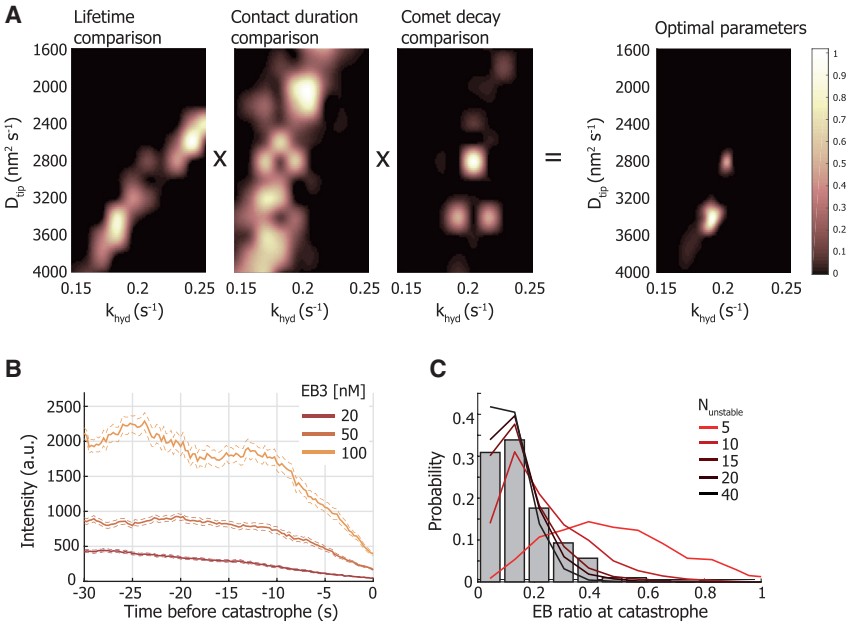

FIGURE 4 Parameter determination of the 1D model. (*A*) The diffusion constant D_{tip} and hydrolysis rate k_{hyd} are determined by comparing the simulated microtubule lifetime distributions, the contact duration distributions, and the decay of the EB signal during contact with the respective experimental distributions. The mean lifetime and contact duration distribution for each simulated pair of D_{tip} and k_{hyd} values is compared with the experimental distribution using a Kolmogorov-Smirnov test. Each comparison yields a similarity parameter, which is displayed in a 2D heatmap. The comparison of the comet decay rate, being a single value, is obtained by evaluating the absolute difference between the simulated rate for each parameter pair and the experimental rate. Evaluating the product of the three heatmaps results in a small range of parameter pairs of D_{tip} and k_{hyd} best describing the experimental data set. The shown heatmaps are for 20 nM EB3. See also Fig. S2. (*B*) The mean experimental EB3 signal during barrier contact, aligned at the moment of catastrophe for 20 ($n = 151$), 50 ($n = 104$), and 100 nM ($n = 92$) EB3. The ratio between the steady-state EB3 signal before catastrophe (from −30 to −15 s) and at the moment of catastrophe is compared with the simulated data in (*C*). The dotted lines denote the SEM. (*C*) Histogram of the ratio between the mean comet intensity during steady-state growth and the comet intensity at the moment of catastrophe. The data are pooled from all experimental data sets of 20, 50, and 100 nM EB3 ($n = 347$). The lines show the simulated GTP/GDP-Pi ratio for $N_{unstable}$ values of 5, 10, 15, 20, and 40. We find that a minimum $N_{unstable}$ value of 15 is required to capture the distribution of pooled experimental EB3 ratios.

test as a measure of the similarity between the simulated and experimental distributions, we obtained heatmaps with (normalized) similarity parameters for each compared distribution (Fig. 4 *A*). We also included a comparison between the simulated GTP/GDP-Pi decay and the experimental EB decay rate during stalling (Fig. 2 *D*). The resulting range of k_{hyd} values that captured the experimental decay rates was used to restrict the range of possible k_{hyd} values for the comparison of simulated and experimental lifetime distributions. The parameter set best capturing all three comparisons was then found by calculating the product between the heatmaps within the range allowed by the decay rates (Figs. 4 *A* and S2).

Determining the catastrophe threshold for the 1D model

To determine the catastrophe threshold governed by $N_{unstable}$, we made use of the experimentally observed decay of the mean EB signal at the barrier (Fig. 2 *D*). Our analysis yielded simultaneous fits of D_{tip} and k_{hyd} that were in very good agreement with our experimental observations across a wide range of $N_{unstable}$ values. To determine an ideal value for $N_{unstable}$ to match our data, we looked at the ratio between the mean EB3 signal during steady-state growth and the EB3 signal at the moment of catastrophe. This would give us a measure of what fraction of GTP/GDP-Pi subunits was on average hydrolyzed at the moment a catastrophe occurred (Fig. 4 *B*). Higher values for $N_{unstable}$ gave rise to a longer stabilizing cap, resulting in a higher ratio of hydrolyzed subunits in the cap at the moment of catastrophe. Comparing the combined distributions of the EB3 ratios with simulated ratios for several $N_{unstable}$ values results in a minimum $N_{unstable}$ value of ∼15 subunits (Fig. 4 *C*).

The 1D model can successfully capture microtubule lifetimes

Fig. 5, *A* and *B* show the experimental cumulative fraction of the lifetimes of freely growing microtubules and of the stalling duration, respectively (*bold lines*), in the presence of 15 μM tubulin and 0, 20, 50, and 100 nM GFP-EB3. The distribution of free lifetimes was determined using microtubules growing parallel to the barriers. By bootstrapping each simulated distribution obtained with the best-fitting parameters (Fig. 5 *C*), we show 25 simulated traces containing an equal number of data points as the experimental data set (*thin lines*). The variability in the simulated distributions provides a good visual reference of the similarity between experiment and simulation (Fig. 5, *A* and *B* and S2). The distributions show that an increasing concentration of EB3 decreases the contact duration (Fig. 5, *B* and *C*). In the absence of EB3 the contact duration is 30.8 ± 1.3 s (median ± SE), whereas in the presence of 20, 50, and 100 nM GFP-EB3 the contact duration is reduced to, respectively, 13.0 ± 0.7, 9.1 ± 0.8, and 4.1 ± 0.3 s (median ± SE). The simulated distributions capture the data well and show that free microtubule lifetimes and microtubule stalling can indeed be

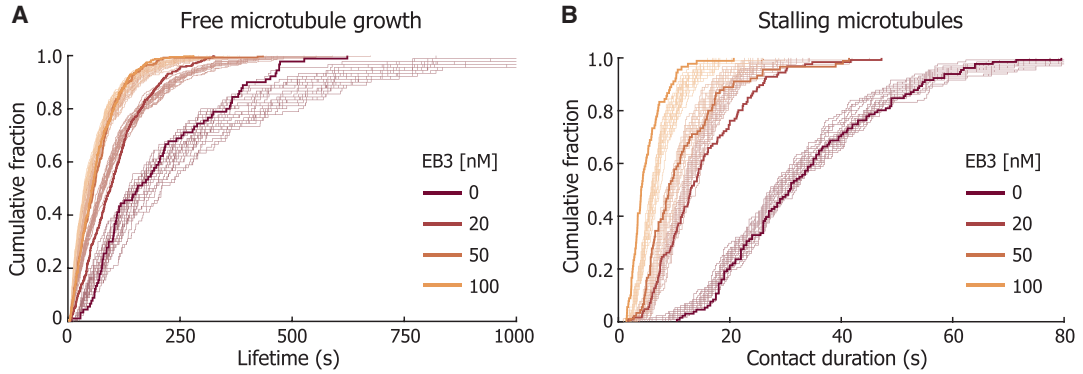

C

EB3	⟨V⟩	k_{hyd}	D_{tip}	Lifetimes experiment		Lifetimes simulation	
				Free	Stalling	Free	Stalling
[nM]	[μm min^{-1}]	[s^{-1}]	[nm^2 s^{-1}]	[s]	[s]	[s]	[s]
0	1.7 ± 0.7	0.07 ± 0.006	3720 ± 310	155 ± 15	30.8 ± 1.3	164 ± 7.4	29.3 ± 0.6
20	2.8 ± 0.9	0.20 ± 0.006	3400 ± 160	94 ± 3.7	13.0 ± 0.7	71.9 ± 3.0	11.7 ± 0.3
50	2.8 ± 0.8	0.24 ± 0.007	3420 ± 141	57 ± 3.5	9.1 ± 0.8	46.3 ± 1.9	9.5 ± 0.2
100	3.7 ± 1.4	0.39 ± 0.007	3100 ± 90	54 ± 2.4	4.1 ± 0.3	39.9 ± 1.8	6.2 ± 0.2

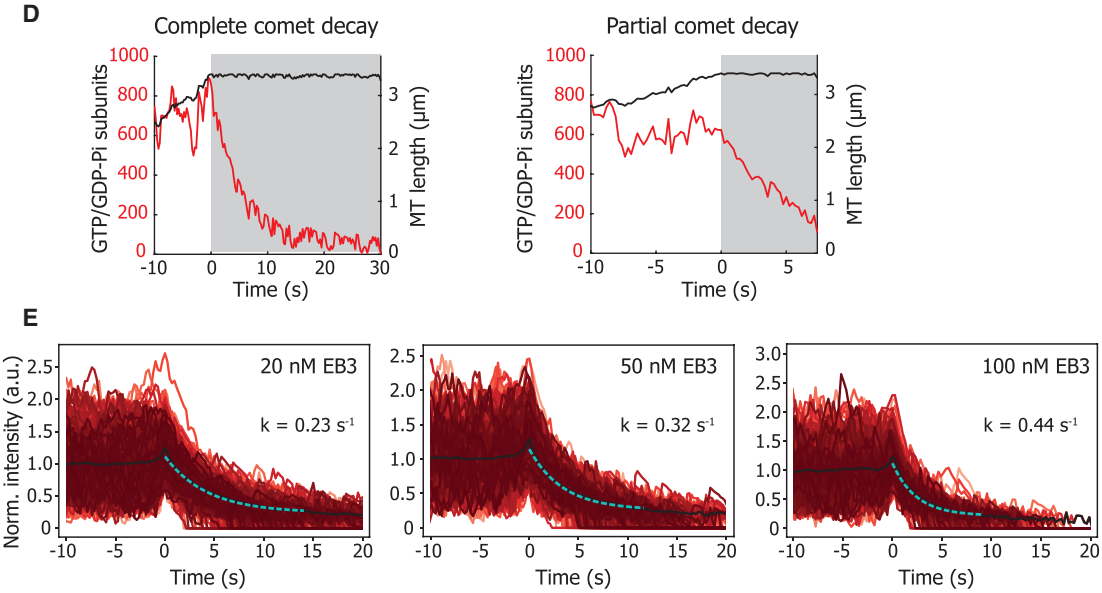

FIGURE 5 Free microtubule growth and microtubule stalling. (*A*) The cumulative fraction of the lifetimes of freely growing microtubules at increasing concentrations of 0 nM ($n = 90$), 20 nM ($n = 384$), 50 nM ($n = 262$), and 100 nM ($n = 398$) EB3. All data were obtained with 15 μM tubulin. The bold lines show the experimental data and the thin lines show 25 bootstrapped simulated distributions of equal number of datapoints as the experimental distribution. (*B*) The cumulative fraction of the microtubule-barrier contact durations at increasing concentrations of 0 nM ($n = 131$), 20 nM ($n = 126$), 50 nM ($n = 90$), and 100 nM ($n = 90$) GFP-EB3. All data were obtained with 15 μM tubulin. The bold lines show the experimental data and the thin lines show 25 bootstrapped simulated distributions of an equal number of datapoints as the experimental distribution. (*C*) Table with the growth velocity $\langle V \rangle$ (mean ± SD), hydrolysis rate k_{hyd} (mean ± 95% CI), and diffusion constant D_{tip} (mean ± 95% CI) as determined to simulate the lifetimes of freely growing microtubules and the contact duration of stalling microtubules at each EB concentration (median ± SE). (*D*) Examples of simulated stalling events, showing the microtubule length and the total number of GTP/GDP-Pi subunits in the lattice. The left trace shows a full comet decay during barrier contact before the onset of a catastrophe, whereas the comet in traces on the right only partially decays. (*E*) Simulated decay of GTP/GDP-Pi subunits during microtubule stalling at increasing EB concentration. Each data set contains 1000 simulated events.

simultaneously captured with a 1D model comprising three parameters (Fig. 5, *A–C*). From the fits, we find that, with increasing EB3 concentration, k_{hyd} increases and D_{tip} decreases (Fig. 5 *C*).

In addition, we find both fully and partially decayed GTP/GDP-Pi intensities at the moment of catastrophe, in agreement with experimentally observed event types (Figs. 5 *D* and 2 *C*). Agreement between the experimental and

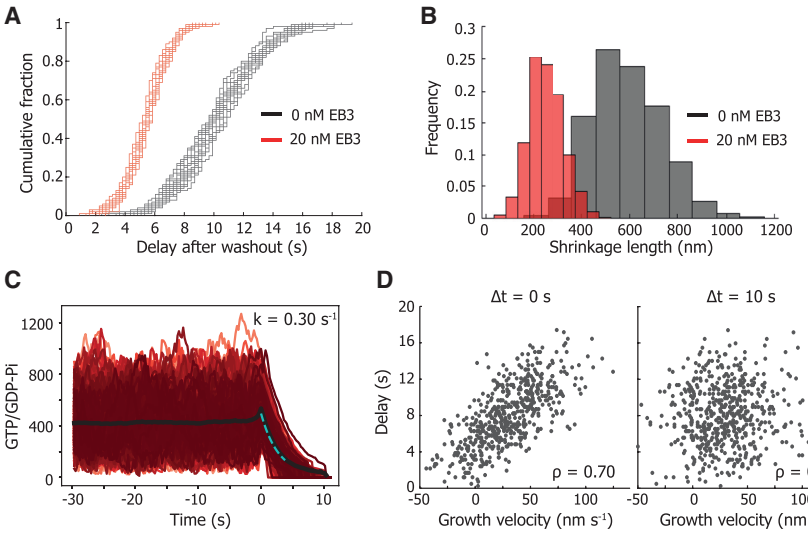

FIGURE 6 Simulating tubulin washout. (*A*) Simulation of tubulin washout following the parameters in Fig. 5 *C* for 0 and 20 nM EB3. For both conditions, 25 bootstrapped distributions of 100 data points are shown. The mean delay duration between washout and catastrophe is 10.3 ± 3.2 and 5.5 ± 1.8 s for 0 and 20 nM EB3, respectively (mean ± SD). (*B*) Simulation of tubulin washout following the parameters in Fig. 5 *C* for 0 and 20 nM EB3. The mean shrinkage length of the microtubule between washout and catastrophe is 588 ± 144 and 253 ± 71 nm, respectively (mean ± SD). (*C*) Simulation of the number of GTP/GDP-Pi subunits before and during tubulin washout following the parameters in Fig. 5 *C* for 20 nM EB3. Fitting the loss of GTP/GDP-Pi subunits from the moment of washout gives a decay rate of 0.30 s^{-1}. (*D*) Scatterplot of the simulated delay time dependency on the growth velocity before tubulin washout. Growth velocities measured immediately before tubulin washout ($\Delta t = 0$ s) show a strong correlation, which is lost for growth velocities measured $\Delta t = 10$ s before washout. The mean growth velocity is calculated from a 10 s time window. ρ is Spearman's rank correlation coefficient.

simulated distributions of the remaining EB3 signal at the moment of catastrophe was found for $N_{unstable} = 15$ (Fig. 4 *C*). The mean decay rate of GTP/GDP-Pi subunits during stalling also matches the experimental data set well and increases with increasing EB3 (Figs. 5 *E* and 2 *D*). The simulated barrier contact events furthermore show a similar noisy comet intensity before catastrophe, confirming that the size of the microtubule stabilizing cap fluctuates with time.

Simulation of tubulin washout

Previous experiments using microfluidics assisted washout of tubulin in vitro have shown that a minimal stable cap has a length of ∼10 tubulin layers at most, of which 15–30% dimers remain unhydrolyzed (32,36,41). The observed delay between tubulin washout and microtubule catastrophe is reported to be ∼7 s (32) and shown to depend on the pre-washout growth velocity (41). To verify the ability of our model to describe tubulin washout experiments, we simulated tubulin washout with our obtained parameter set (Fig. 5 *C*). To simulate washout, we prohibit any growth of the microtubule tip after 40 s, but still allow microtubules to undergo negative growth excursions (Fig. 3 *B*). To compare our results with published washout parameters (20 μM tubulin with 0 and 200 nM of Mal3) (41), we simulate tubulin washout for 15 μM tubulin in the presence of 0 and 20 nM EB3, resulting in a comparable growth velocity and hydrolysis rate. The difference between the concentration of Mal3 (fission yeast homolog of EB1) and EB3 required to obtain a similar hydrolysis rate can be explained by the intrinsic structural differences (84,85). Our simulation of tubulin washout showed a delay between washout and catastrophe of 10.2 ± 3.2 and 5.5 ± 1.8 s (mean ± SD) for 0 and 20 nM EB3 (Fig. 6 *A*), similar to the reported values of 7.3 and 3.5 s for 0 and 200 nM Mal3 (41). In addition, it was reported that microtubule growth is not simply paused after washout, but that microtubules slowly shrank before catastrophe. During the simulated washout delay, we measured a slow decrease in microtubule length of 253 ± 71 nm (mean ± SD) for 20 nM EB3 (Fig. 6 *B*), comparable with the reported 165 ± 105 nm for 200 nM Mal3 (41). Furthermore, we find that the simulated decay rate of 0.30 s^{-1} (20 nM EB3) of GTP/GDP-Pi subunits from the moment of tubulin washout is in agreement with the reported 0.33 s^{-1} (200 nM Mal3) (Fig. 6 *C*).

Our simulated data also capture the reported positive correlation between microtubule stability and growth velocity (Fig. 6 *D*) (41). The simulated washout delay increases with an increasing growth velocity as measured immediately before washout (Spearman's correlation coefficient of $\rho = 0.70$). However, the correlation is lost when the growth velocity is measured 10 s before washout ($\rho = 0.07$), in agreement with published results (41). We conclude that our model is thus capable of accurately capturing tubulin washout experiments.

The 1D model successfully captures the mild catastrophe dependence on microtubule growth rates

As an additional verification of our model, we simulated microtubule lifetimes and stalling durations based on our previous experimental data (Fig. 7) (42). Our model can simultaneously capture the reported mild reduction in catastrophe rate with increasing growth velocity as well as the distribution of stalling durations (Fig. 7, *A* and *B*). To explain these data, we had to assume a velocity-dependent tip noise (at a fixed k_{hyd} of 0.10 s^{-1}), which is in line with the reported linear dependence of the tip noise on the growth

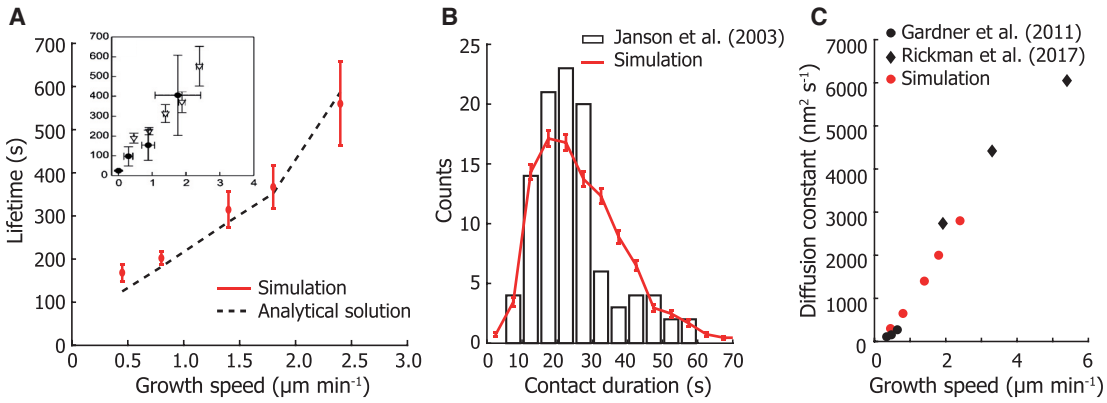

FIGURE 7 Model evaluation. (*A*) Simulation of microtubule lifetimes for increasing growth velocities. The simulation growth velocities were obtained from (42) and combined with a global value for k_{hyd} of 0.10 s^{-1} and the determined $N_{unstable}$ of 15. The insert shows the experimental lifetimes for freely growing microtubules (*triangles*) and for buckling microtubules (*dots*) (42). Our simulation gives a similarly mild suppression of catastrophes with increasing tubulin concentrations, with the growth velocities of 0.45, 0.8, 1.4, 1.8, and 2.4 μm min^{-1} corresponding to tubulin concentrations of 7.2 ($n = 58$), 10 ($n = 152$), 15.2 ($n = 49$), 20 ($n = 51$), and 28 μM ($n = 30$). Simulated lifetimes are given as mean ± SE with the same number of data points as the experimental values. The mild catastrophe suppression is also captured by the analytical solution of our model (see materials and methods). (*B*) Histogram of the pooled stalling duration with 103 events measured at 15.2, 20, and 28 μM from (42) and the simulated stalling duration. The simulated values represent mean ± SD for $n = 103$ events. (*C*) The diffusion constant of the microtubule tip required to simulate the microtubule lifetimes in (*A*) based on data from (42). These values follow a linear dependence on the growth speed which is in agreement with previously reported results (21,24).

velocity both in the absence and presence of Mal3 (Fig. 7 *C*) (21,24). This relationship shows a linear dependence of the tip noise on the growth velocity, as has been developed for a 1D model (21,24):

$$D_{tip} = \frac{a}{2}\frac{k_a + k_d}{k_a - k_d}\langle V\rangle$$

where a is the size of a dimer, k_a the tubulin addition rate, and k_d the tubulin dissociation rate. We thus conclude that our 1D model can describe the reported mild dependence of the microtubule lifetimes on the growth velocity.

DISCUSSION

EB3 enhances catastrophes for stalling microtubules

Using novel microfabricated barriers in conjunction with TIRF microscopy, we studied the duration of barrier contact as well as the dynamics of the EB3 comet during microtubule stalling. We confirm that stalled microtubules undergo a catastrophe after 30.8 ± 1.3 s (median ± SE) in the absence of EB3, comparable with previously measured values (Fig. 7 *B*) (42). The presence of EB3 further enhances catastrophes in a concentration-dependent manner, which results in up to five times shorter microtubule contact times at the barriers (Fig. 5, *A–C*). In earlier unpublished experiments, we made similar observations for stalling microtubules in the presence of Mal3 (Fig. S4). These shorter contact times are accompanied by an increase in the decay rate of the EB3 comet (Fig. 2 *D*).

In addition, we developed a simple phenomenological computational model that predicts catastrophe statistics based on parameters related to random (uncoupled) GTP hydrolysis and fluctuations in microtubule growth. Fitting the model to the data suggests that the size of the growth fluctuations (D_{tip}) decreases in the presence of EB3 (Fig. 5 *C*). This effect would support the hypothesis that the increase in growth velocity due to the presence of EB3 is the result of a lower tubulin dissociation rate at the microtubule tip. If we assume that the tubulin association rate at the microtubule tip only depends on the soluble tubulin concentration and is therefore not affected by EB3, we would indeed expect the resulting tip noise D_{tip} to be smaller with increasing concentrations of EB3. This effect could originate from EB3 binding in between protofilaments and reducing tip fluctuations or from the hypothesis that EB3 increases the growth velocity by closing the lattice seam (1).

A 1D phenomenological model successfully describes microtubule lifetimes, stalling, and tubulin washout

We developed a simple phenomenological computational model that can capture a very rich set of experimental data on dynamic microtubules. Its sole dependence on (velocity dependent) tip noise and random hydrolysis makes it possible to build an intuition of key processes in microtubule dynamics, in particular the onset of catastrophe. We find that our model can reproduce both the experimental microtubule stalling duration and the accompanying EB comet decay rate (Fig. 5). At the same time, our model captures the reported mild reduction in catastrophe rate with increasing growth velocity as well as the distribution of stalling durations (Fig. 7, *A* and *B*). Previous 1D models were not able to describe both the mild catastrophe

dependence on microtubule growth rates and the size of the stabilizing cap (35,64). A reason for this was the assumption that tubulin dissociation is independent from the microtubule growth velocity (55). This necessitated introducing lateral tubulin-tubulin interactions in a 2D model to accurately capture microtubule lifetimes and cap dynamics (21,35). Here, we showed that introducing a highly dynamic tip in a 1D model is sufficient to accurately capture both the microtubule lifetimes as well as the size of the stabilizing cap. The magnitude of the required simulated tip noise would not be observable using fluorescence microscopy, but only with optical tweezers (21–23). The extent of any "blurring" of the microtubule tip due to tip noise during frame acquisition would remain below the observable optical resolution (Fig. S6 *D*).

We furthermore showed that our model can capture tubulin washout and reproduce a similar catastrophe delay, tip shrinkage, and comet decay as previously reported (Fig. 6) (36,41). Our model also produces the same correlation between washout delays and growth velocity as was previously observed experimentally (41) and thus captures the reported momentary nature of microtubule stability. We conclude that our model can describe tubulin washout and reproduce values in good agreement with experiments.

Microtubule stability depends on the distribution of hydrolyzed dimers at the tip

The decay of the EB3 comet during barrier contact can provide further insights into the criterion for microtubule stability. We find that microtubules can remain in a stalled state without the presence of an observable EB3 comet both in our experiments and simulations (compare Figs. 2 *C* and 5 *D*). This suggests that a stalled microtubule does not necessarily require a number of GTP/GDP-Pi subunits that is large enough to be observed as a comet. The effect is explained by the presence of growth fluctuations during microtubule stalling. Hydrolyzed subunits at the tip are continually replaced by newly incorporated unhydrolyzed subunits, reducing the probability of reaching the critical threshold of $N_{unstable}$ at the microtubule tip. This phenomenon could also account for reported pausing events during which a microtubule temporarily stops growing without triggering a catastrophe (57). It illustrates that the onset of a catastrophe is not fully coupled to the presence of an observable comet.

To determine the stretch of hydrolyzed subunits at the microtubule tip required to initiate a catastrophe ($N_{unstable}$), we measured the ratio between the EB3 comet intensity at the moment of catastrophe and the mean EB3 comet intensity during steady-state growth (Fig. 4, *B* and *C*). In parallel, we evaluated the decay rates of EB3 comets after initial barrier contact. Both measures converge on a catastrophe threshold $N_{unstable}$ of ∼15 uninterrupted hydrolyzed terminal subunits, which would approximate a single tubulin layer at the tip of a real 3D microtubule, in line with experimental observations (33,37). A previous finding from washout experiments showing that a microtubule requires a stable cap of ∼10 tubulin layers at most (41) is not at odds with our finding that a catastrophe is triggered when the terminal layer of tubulin is hydrolyzed. Because the former result is based on the average remaining density of Mal3 at the moment of catastrophe after tubulin washout, it does not inform on a specific catastrophe criterion. The notion that the stabilizing cap (L_{cap}) and the EB3 comet (GTP/GDP-Pi region) are large on average, but that only a short stretch of hydrolyzed subunits at the microtubule tip is required to trigger a catastrophe, reconciles short and long cap observations (32,35,36,38,41,61). We thus find that the stability of a microtubule does not primarily depend on the size of the observed EB comet, but instead on the underlying distribution of hydrolyzed subunits at the microtubule tip.

Both the cap size and tip fluctuations determine the onset of catastrophe

To better understand the size of the stabilizing cap (L_{cap}) and its effect on the catastrophe frequency, we derived an analytical expression for the position of the sequence of hydrolyzed subunits equal to or greater than $N_{unstable}$ (see materials and methods for details). This position is determined by $N_{unstable}$ and the underlying distribution of hydrolyzed subunits. We assume that the density of unhydrolyzed dimers decreases exponentially along the microtubule lattice and is fully characterized by k_{hyd} and $\langle V \rangle$ (38,41,79). By treating the microtubule lattice as a series of independent Bernoulli trials, we can obtain an expression for the mean position of the first occurrence of a series of hydrolyzed subunits equal to or greater than $N_{unstable}$ (Figs. 8 *A* and S5, *A* and *B*). The distance between the microtubule tip and this position is equal to the size of the stabilizing cap, which means we can obtain the relation between the size of the stabilizing cap and the parameters $N_{unstable}$, k_{hyd}, and $\langle V \rangle$ (Figs. 8, *B* and *C* and S5 *B*). We find that the size of the stabilizing cap scales linearly with the growth velocity $\langle V \rangle$ (Fig. 8 *B*). The addition of EB3, however, affects both the growth velocity and the hydrolysis rate, the combined effect of which results in a decreasing cap size with increasing EB concentration (Fig. 8 *C*). We can calculate the mean size of the stabilizing cap in our model based on k_{hyd}, $\langle V \rangle$, and $N_{unstable}$ and compare it with the length of the GTP/GDP-Pi region for which the EB comet signal is a proxy. Taking $L_{comet} = \frac{\langle V \rangle}{k_{hyd}}$ as the characteristic length of the EB comet (24,41), we find that the comet underestimates the size of the calculated stabilizing cap (Fig. 8 *C*).

Having an expression for the size of the stabilizing cap, we can now explore an intuitive view on how a catastrophe

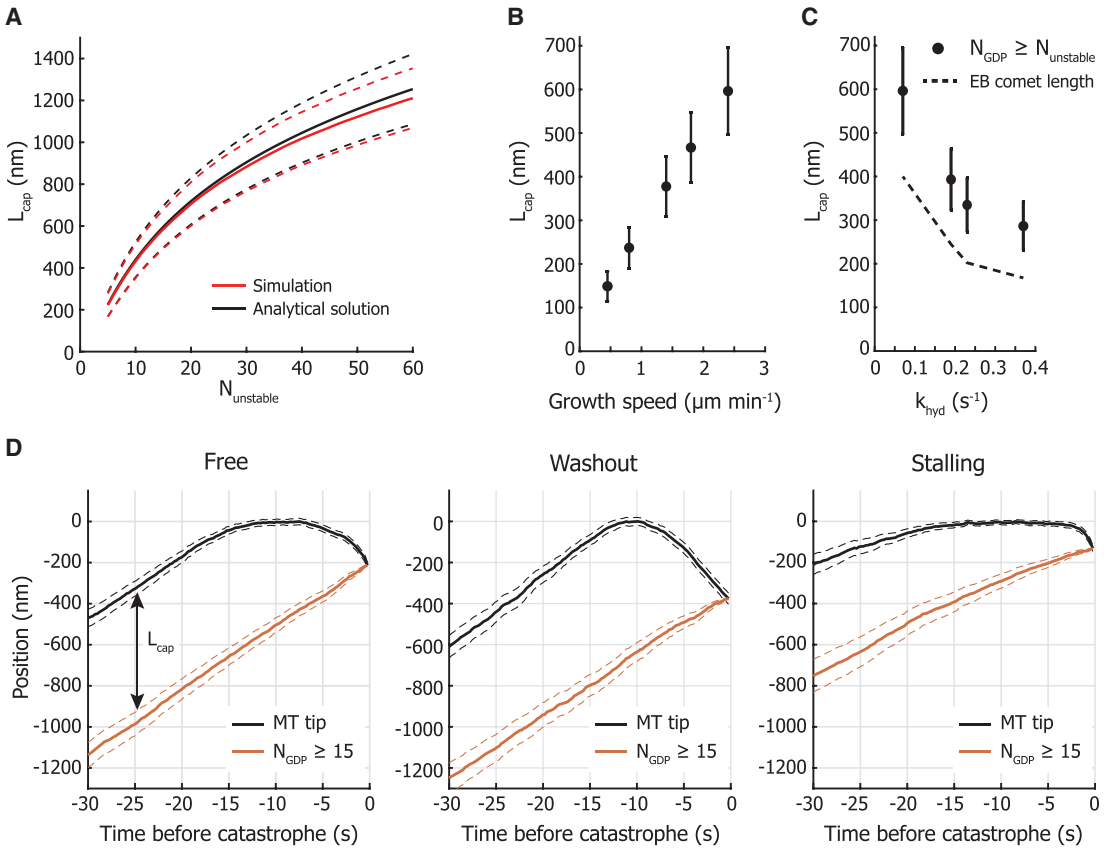

FIGURE 8 Fluctuations of the stabilizing cap trigger catastrophes. (*A*) Dependence of the cap length L_{cap} on $N_{unstable}$ (mean ± SD). The simulated cap length and the numerical solution based on the analytical model are in good agreement. The shown cap length was determined for the parameters of 0 nM EB3 in Fig. 5 *C*. (*B*) The length of the stabilizing cap L_{cap} depends linearly on the growth velocity $\langle V \rangle$. The cap length was calculated with the analytical model (mean ± SD) and required a constant k_{hyd} of 0.1 s^{-1} and an $N_{unstable}$ of 15, equal to the simulation parameters based on the data from (42) (see Fig. 7 *B*). (*C*) The mean length of the stabilizing cap L_{cap} decreases with increasing hydrolysis rate k_{hyd}. The dependence of the cap size on the hydrolysis rate is calculated with the analytical model (mean ± SD) and is based on the parameters of the EB concentrations 0, 20, 50, and 100 nM in Fig. 5 *C*. The size of the stabilizing cap based on the position of the sequence $N_{unstable}$ is larger than the stabilizing cap based on the characteristic length of the EB signal (GTP/GDP-Pi region). (*D*) Simulation of the position of the microtubule tip and of the position of the sequence of hydrolyzed subunits defined by $N_{unstable} = 15$ before catastrophe. Mean traces are for catastrophes during microtubule free growth, after tubulin washout, and during microtubule stalling (mean ± SE). Before the onset of catastrophe, the mean cap length L_{cap} is constant during steady-state growth as both the position of the tip and the end of the cap move with equal velocity $\langle V \rangle$. A catastrophe is triggered when $L_{cap} = 0$, which is predominantly determined by persistent negative growth excursions of the microtubule tip. All simulations were performed with the parameters for 0 nM EB (Fig. 5 *C*).

is triggered. The length of the cap is determined by two competing processes on either end, namely noisy growth at the microtubule tip and hydrolysis in the lattice. During steady-state growth, the mean length of the stabilizing cap has a constant size determined by the growth velocity $\langle V \rangle$ and hydrolysis rate k_{hyd} (41). We observe in our simulations that catastrophes for freely growing microtubules occur as a result of a short period of slowed down or negative growth (Figs. 8 *D*, *left* and S3 *C*), in agreement with previous experimental observations (86) (also compare Fig. S3 with Fig. 7 in (79)). This shows that the onset of catastrophe is determined by the probability that growth fluctuations remove the stabilizing cap. When we treat the probability for a catastrophe as the probability for negative growth excursions to exceed the length of the stabilizing cap, the microtubule lifetimes are successfully reproduced with the analytical solution (Figs. 7 *A* and S5 *D*). This holds true for catastrophes during free growth and after tubulin washout (Fig. 8 *D*, *left* and *middle*). During microtubule stalling, however, continuing tip fluctuations replace hydrolyzed subunits at the tip for unhydrolyzed subunits, reducing the effective mean hydrolysis rate. This results in slowing down of the cap end and delaying the onset of catastrophe (Fig. 8 *D*, *right*). In addition, the longer catastrophe delay observed with microtubule stalling compared with tubulin washout can be explained by the different effective tip fluctuations. After tubulin washout, loss of the stabilizing cap is caused by both continued hydrolysis and the irreversible loss of tubulin subunits at the tip, whereas the tip of a stalling microtubule can still recover after loss of terminal subunits through tubulin addition and continue to fluctuate (Fig. 8 *D*).

Multistep microtubule catastrophes are not required to describe microtubule lifetimes

An experimentally observed feature of microtubule stability that is not reproduced by our model is an age-dependent catastrophe frequency. It has been reported that "younger" microtubules are more stable than "older" ones (69,70). Aging has also been observed through a gradual reduction of the EB comet intensity during steady-state growth (87,88) and through shorter catastrophe delays after tubulin washout for older microtubules (68). The two proposed mechanisms responsible for aging are based on a multistep catastrophe process (55,87,89) or on progressive tapering of the microtubule tip during growth (57,58,68,90). In our 1D model, however, the onset of a catastrophe is independent from microtubule age. This leads to a modest discrepancy where, in the experimental lifetime distributions of free microtubules, there is an apparent lack of short events (<50 s) compared with the simulated curves, especially in the absence of EB3 (Fig. 5 *A*).

Microtubule aging is often characterized by fitting a Gamma distribution to lifetime distributions to obtain the shape parameter, a measure for the number of sequential steps required to trigger a catastrophe within the view of a multistep catastrophe process (69,70). For our experimental lifetime distributions, we find that the Gamma shape parameter in such an analysis is around 2 and independent from the EB concentration (Fig. S6 *A*), in line with previous reports (87). To account for apparent microtubule aging in our model, we introduced time-dependent tip fluctuations (Fig. S6 *B*). Increasing the growth fluctuations with time, while keeping the mean growth velocity constant, increases the probability of reducing the stabilizing cap to zero due to an increase in negative growth excursions for longer microtubules. By increasing D_{tip} from an initially low value to a higher constant value following a bounded exponential curve (with a rate of 0.025 s^{-1}), we can reproduce the experimental aging parameters (Fig. S6 *C*) without the need for a multistep catastrophe process. Linking microtubule aging to an increase in tip noise may relate to the observation of progressive tapering of microtubule ends and may also resonate with previous (59) reports that microtubule aging is correlated with the frequency of encountering curled protofilaments (59,60).

CONCLUSION

Our experimental setup will be useful for studying microtubule interactions with, and the functional effect of, stabilizing and destabilizing microtubule-associated proteins. Our approach can be used to study the influence of microtubule associated proteins (MAPs) (91), tubulin isotypes, and post translational modifications (PTMs) (92,93) on the stability of pushing microtubules. Furthermore, the SiC overhangs are designed to be compatible with a previously published method to specifically functionalize the barriers with protein complexes (72), enabling the study of microtubule end-on interactions with TIRF microscopy (18).

A possible extension of our 1D model to describe the effect of +TIPs on microtubule dynamics could be to characterize them phenomenologically by their effect on GTP hydrolysis and tip fluctuations. As the effect of EB3 can be described this way, we hypothesize that the effect of other microtubule-associated proteins can be characterized similarly. For example, for XMAP215, it was shown that catastrophes are increased because of large fluctuations in growth velocity rather than an effect on the GTP hydrolysis rate (94). To allow future extensions and modifications of our model, we have made the simulation source code available under an open-source licence on GitHub (https://github.com/florian-huber/mtdynamics) with extra documentation.

ACKNOWLEDGMENTS

We thank M.O. Steinmetz for the gift of GFP-EB3 and the technicians of the van Leeuwenhoek Laboratory for their technical assistance in the fabrication of the barriers. We thank Vladimir Volkov, Louis Reese, and Reza Amini for discussions and critical reading of the manuscript and Seungkyu Ha for his assistance in acquiring the SEM images. This work was supported by the European Research Council Synergy grant 6098822 to M.D.

AUTHOR CONTRIBUTIONS

M.K. designed and fabricated the microfabricated barriers, performed experiments with EB, analyzed the data, developed the analytical solution, and ran simulations. F.H. developed the 1D microtubule model, wrote the simulation code, and ran the simulations. S.-M.K. performed and analyzed the experiments with Mal3. M.K., F.H., and M.D. wrote the paper. M.D. coordinated the project.

DECLARATION OF INTERESTS

The authors declare no competing financial interests.

SUPPORTING MATERIAL

Supporting material can be found online at https://doi.org/10.1016/j.bpj.2024.11.3314.

REFERENCES

1. Zhang, R., G. M. Alushin, …, E. Nogales. 2015. Mechanistic Origin of Microtubule Dynamic Instability and Its Modulation by EB Proteins. *Cell.* 162:849–859. https://doi.org/10.1016/j.cell.2015.07.012.
2. Tilney, L. G., J. Bryan, …, D. H. Snyder. 1973. Microtubules: evidence for 13 protofilaments. *J. Cell Biol.* 59:267–275. https://doi.org/10.1083/jcb.59.2.267.
3. Debs, G. E., M. Cha, …, C. V. Sindelar. 2020. Dynamic and asymmetric fluctuations in the microtubule wall captured by high-resolution cryoelectron microscopy. *Proc. Natl. Acad. Sci. USA.* 117:16976–16984. https://doi.org/10.1073/pnas.2001546117.
4. Mitchison, T., and M. Kirschner. 1984. Dynamic instability of microtubule growth. *Nature.* 312:237–242.

5. Akhmanova, A., and M. O. Steinmetz. 2015. Control of microtubule organization and dynamics: two ends in the limelight. *Nat. Rev. Mol. Cell Biol.* 16:711–726. https://doi.org/10.1038/nrm4084.
6. Colin, A., P. Singaravelu, …, Z. Gueroui. 2018. Actin-Network Architecture Regulates Microtubule Dynamics. *Curr. Biol.* 28:2647–2656.e4. https://doi.org/10.1016/j.cub.2018.06.028.
7. Dogterom, M., and G. H. Koenderink. 2019. Actin-microtubule crosstalk in cell biology. *Nat. Rev. Mol. Cell Biol.* 20:38–54. https://doi.org/10.1038/s41580-018-0067-1.
8. Preciado Lopez, M., F. Huber, …, M. Dogterom. 2014. Actin-microtubule coordination at growing microtubule ends. *Nat. Commun.* 5:4778. https://doi.org/10.1038/ncomms5778.
9. Gurel, P. S., A. L. Hatch, and H. N. Higgs. 2014. Connecting the cytoskeleton to the endoplasmic reticulum and Golgi. *Curr. Biol.* 24:R660–R672. https://doi.org/10.1016/j.cub.2014.05.033.
10. Waterman-Storer, C. M., J. Gregory, …, E. D. Salmon. 1995. Membrane/microtubule tip attachment complexes (TACs) allow the assembly dynamics of plus ends to push and pull membranes into tubulovesicular networks in interphase Xenopus egg extracts. *J. Cell Biol.* 130:1161–1169. https://doi.org/10.1083/jcb.130.5.1161.
11. Nguyen-Ngoc, T., K. Afshar, and P. Gönczy. 2007. Coupling of cortical dynein and Gα proteins mediates spindle positioning in Caenorhabditis elegans. *Nat. Cell Biol.* 9:1294–1302. https://doi.org/10.1038/ncb1649.
12. Komarova, Y. A., I. A. Vorobjev, and G. G. Borisy. 2002. Life cycle of MTs: persistent growth in the cell interior, asymmetric transition frequencies and effects of the cell boundary. *J. Cell Sci.* 115:3527–3539.
13. Tischer, C., D. Brunner, and M. Dogterom. 2009. Force- and kinesin-8-dependent effects in the spatial regulation of fission yeast microtubule dynamics. *Mol. Syst. Biol.* 5:250. https://doi.org/10.1038/msb.2009.5.
14. Gregoretti, I. V., G. Margolin, …, H. V. Goodson. 2006. Insights into cytoskeletal behavior from computational modeling of dynamic microtubules in a cell-like environment. *J. Cell Sci.* 119:4781–4788. https://doi.org/10.1242/jcs.03240.
15. Letort, G., F. Nedelec, …, M. Théry. 2016. Centrosome centering and decentering by microtubule network rearrangement. *Mol. Biol. Cell.* 27:2833–2843. https://doi.org/10.1091/mbc.E16-06-0395.
16. Bouchet, B. P., I. Noordstra, …, A. Akhmanova. 2016. Mesenchymal Cell Invasion Requires Cooperative Regulation of Persistent Microtubule Growth by SLAIN2 and CLASP1. *Dev. Cell.* 39:708–723. https://doi.org/10.1016/j.devcel.2016.11.009.
17. Brangwynne, C. P., F. C. MacKintosh, …, D. A. Weitz. 2006. Microtubules can bear enhanced compressive loads in living cells because of lateral reinforcement. *J. Cell Biol.* 173:733–741. https://doi.org/10.1083/jcb.200601060.
18. Vleugel, M., M. Kok, and M. Dogterom. 2016. Understanding force-generating microtubule systems through in vitro reconstitution. *Cell Adhes. Migrat.* 10:475–494. https://doi.org/10.1080/19336918.2016.1241923.
19. Carlier, M. F., and D. Pantaloni. 1982. Assembly of microtubule protein: role of guanosine di- and triphosphate nucleotides. *Biochemistry.* 21:1215–1224. https://www.ncbi.nlm.nih.gov/pubmed/7074077.
20. Nogales, E. 1999. A structural view of microtubule dynamics. *Cell. Mol. Life Sci.* 56:133–142. http://www.ncbi.nlm.nih.gov/pubmed/11213253.
21. Gardner, M. K., B. D. Charlebois, …, D. J. Odde. 2011. Rapid microtubule self-assembly kinetics. *Cell.* 146:582–592. https://doi.org/10.1016/j.cell.2011.06.053.
22. Kerssemakers, J. W. J., E. L. Munteanu, …, M. Dogterom. 2006. Assembly dynamics of microtubules at molecular resolution. *Nature.* 442:709–712. https://doi.org/10.1038/nature04928.
23. Schek, H. T., 3rd, M. K. Gardner, …, A. J. Hunt. 2007. Microtubule assembly dynamics at the nanoscale. *Curr. Biol.* 17:1445–1455. https://doi.org/10.1016/j.cub.2007.07.011.
24. Rickman, J., C. Duellberg, …, T. Surrey. 2017. Steady-state EB cap size fluctuations are determined by stochastic microtubule growth and maturation. *Proc. Natl. Acad. Sci. USA.* 114:3427–3432. https://doi.org/10.1073/pnas.1620274114.
25. Mickolajczyk, K. J., E. A. Geyer, …, W. O. Hancock. 2019. Direct observation of individual tubulin dimers binding to growing microtubules. *Proc. Natl. Acad. Sci. USA.* 116:7314–7322. https://doi.org/10.1073/pnas.1815823116.
26. Alushin, G. M., G. C. Lander, …, E. Nogales. 2014. High-resolution microtubule structures reveal the structural transitions in αβ-tubulin upon GTP hydrolysis. *Cell.* 157:1117–1129. https://doi.org/10.1016/j.cell.2014.03.053.
27. Carlier, M. F., and D. Pantaloni. 1981. Kinetic analysis of guanosine 5'-triphosphate hydrolysis associated with tubulin polymerization. *Biochemistry.* 20:1918–1924. http://www.ncbi.nlm.nih.gov/pubmed/7225365.
28. Brouhard, G. J., and L. M. Rice. 2018. Microtubule dynamics: an interplay of biochemistry and mechanics. *Nat. Rev. Mol. Cell Biol.* 19:451–463. https://doi.org/10.1038/s41580-018-0009-y.
29. Ohi, R., and M. Zanic. 2016. Ahead of the Curve: New Insights into Microtubule Dynamics. *F1000Res.* 5:F1000. https://doi.org/10.12688/f1000research.7439.1.
30. Gudimchuk, N. B., and J. R. McIntosh. 2021. Regulation of microtubule dynamics, mechanics and function through the growing tip. *Nat. Rev. Mol. Cell Biol.* 22:777–795. https://doi.org/10.1038/s41580-021-00399-x.
31. Farmer, V. J., and M. Zanic. 2023. Beyond the GTP-cap: Elucidating the molecular mechanisms of microtubule catastrophe. *Bioessays.* 45:e2200081. https://doi.org/10.1002/bies.202200081.
32. Walker, R. A., N. K. Pryer, and E. D. Salmon. 1991. Dilution of individual microtubules observed in real time in vitro: evidence that cap size is small and independent of elongation rate. *J. Cell Biol.* 114:73–81. https://doi.org/10.1083/jcb.114.1.73.
33. Caplow, M., and J. Shanks. 1996. Evidence that a single monolayer tubulin-GTP cap is both necessary and sufficient to stabilize microtubules. *Mol. Biol. Cell.* 7:663–675. https://doi.org/10.1091/mbc.7.4.663.
34. Karr, T. L., and D. L. Purich. 1978. Examination of tubulin-nucleotide interactions by protein fluorescence quenching measurements. *Biochem. Biophys. Res. Commun.* 84:957–961. https://www.ncbi.nlm.nih.gov/pubmed/728162.
35. Brun, L., B. Rupp, …, F. Nédélec. 2009. A theory of microtubule catastrophes and their regulation. *Proc. Natl. Acad. Sci. USA.* 106:21173–21178. https://doi.org/10.1073/pnas.0910774106.
36. Voter, W. A., E. T. O'Brien, and H. P. Erickson. 1991. Dilution-induced disassembly of microtubules: relation to dynamic instability and the {GTP} cap. *Cell Motil Cytoskeleton.* 18:55–62. https://doi.org/10.1002/cm.970180106.
37. Drechsel, D. N., and M. W. Kirschner. 1994. The minimum GTP cap required to stabilize microtubules. *Curr. Biol.* 4:1053–1061. https://doi.org/10.1016/s0960-9822(00)00243-8.
38. Seetapun, D., B. T. Castle, …, D. J. Odde. 2012. Estimating the microtubule GTP cap size in vivo. *Curr. Biol.* 22:1681–1687. https://doi.org/10.1016/j.cub.2012.06.068.
39. Maurer, S. P., P. Bieling, …, T. Surrey. 2011. GTPγS microtubules mimic the growing microtubule end structure recognized by end-binding proteins (EBs). *Proc. Natl. Acad. Sci. USA.* 108:3988–3993. https://doi.org/10.1073/pnas.1014758108.
40. Roostalu, J., C. Thomas, …, T. Surrey. 2020. The speed of GTP hydrolysis determines GTP cap size and controls microtubule stability. *Elife.* 9:e51992. https://doi.org/10.7554/eLife.51992.
41. Duellberg, C., N. I. Cade, …, T. Surrey. 2016. The size of the EB cap determines instantaneous microtubule stability. *Elife.* 5:e13470. https://doi.org/10.7554/eLife.13470.
42. Janson, M. E., M. E. de Dood, and M. Dogterom. 2003. Dynamic instability of microtubules is regulated by force. *J. Cell Biol.* 161:1029–1034. https://doi.org/10.1083/jcb.200301147.

43. Odde, D. J., L. Ma, …, M. W. Kirschner. 1999. Microtubule bending and breaking in living fibroblast cells. *J. Cell Sci.* 112:3283–3288. https://www.ncbi.nlm.nih.gov/pubmed/10504333.

44. Pallavicini, C., A. Monastra, …, L. Bruno. 2017. Characterization of microtubule buckling in living cells. *Eur. Biophys. J.* 46:581–594. https://doi.org/10.1007/s00249-017-1207-9.

45. Brangwynne, C. P., F. C. MacKintosh, and D. A. Weitz. 2007. Force fluctuations and polymerization dynamics of intracellular microtubules. *Proc. Natl. Acad. Sci. USA.* 104:16128–16133. https://doi.org/10.1073/pnas.0703094104.

46. Das, D., D. Das, and R. Padinhateeri. 2014. Force-induced dynamical properties of multiple cytoskeletal filaments are distinct from that of single filaments. *PLoS One.* 9:e114014. https://doi.org/10.1371/journal.pone.0114014.

47. Valiyakath, J., and M. Gopalakrishnan. 2018. Polymerisation force of a rigid filament bundle: diffusive interaction leads to sublinear force-number scaling. *Sci. Rep.* 8:2526. https://doi.org/10.1038/s41598-018-20259-7.

48. Laan, L., J. Husson, …, M. Dogterom. 2008. Force-generation and dynamic instability of microtubule bundles. *Proc. Natl. Acad. Sci. USA.* 105:8920–8925. https://doi.org/10.1073/pnas.0710311105.

49. Chen, Y. D., and T. L. Hill. 1985. Monte Carlo study of the GTP cap in a five-start helix model of a microtubule. *Proc. Natl. Acad. Sci. USA.* 82:1131–1135. https://www.ncbi.nlm.nih.gov/pubmed/3856250.

50. Bayley, P., M. Schilstra, and S. Martin. 1989. A lateral cap model of microtubule dynamic instability. *FEBS Lett.* 259:181–184. https://doi.org/10.1016/0014-5793(89)81523-6.

51. VanBuren, V., D. J. Odde, and L. Cassimeris. 2002. Estimates of lateral and longitudinal bond energies within the microtubule lattice. *Proc. Natl. Acad. Sci. USA.* 99:6035–6040. https://doi.org/10.1073/pnas.092504999.

52. Padinhateeri, R., A. B. Kolomeisky, and D. Lacoste. 2012. Random hydrolysis controls the dynamic instability of microtubules. *Biophys. J.* 102:1274–1283. https://doi.org/10.1016/j.bpj.2011.12.059.

53. Margolin, G., I. V. Gregoretti, …, H. V. Goodson. 2012. The mechanisms of microtubule catastrophe and rescue: implications from analysis of a dimer-scale computational model. *Mol. Biol. Cell.* 23:642–656. https://doi.org/10.1091/mbc.E11-08-0688.

54. Piedra, F. A., T. Kim, …, L. M. Rice. 2016. GDP-to-GTP exchange on the microtubule end can contribute to the frequency of catastrophe. *Mol. Biol. Cell.* 27:3515–3525. https://doi.org/10.1091/mbc.E16-03-0199.

55. Bowne-Anderson, H., M. Zanic, …, J. Howard. 2013. Microtubule dynamic instability: a new model with coupled GTP hydrolysis and multistep catastrophe. *Bioessays.* 35:452–461. https://doi.org/10.1002/bies.201200131.

56. Lee, C. T., and E. M. Terentjev. 2019. Structural effects of cap, crack, and intrinsic curvature on the microtubule catastrophe kinetics. *J. Chem. Phys.* 151:135101. https://doi.org/10.1063/1.5122304.

57. VanBuren, V., L. Cassimeris, and D. J. Odde. 2005. Mechanochemical model of microtubule structure and self-assembly kinetics. *Biophys. J.* 89:2911–2926. https://doi.org/10.1529/biophysj.105.060913.

58. Coombes, C. E., A. Yamamoto, …, M. K. Gardner. 2013. Evolving tip structures can explain age-dependent microtubule catastrophe. *Curr. Biol.* 23:1342–1348. https://doi.org/10.1016/j.cub.2013.05.059.

59. Zakharov, P., N. Gudimchuk, …, E. L. Grishchuk. 2015. Molecular and Mechanical Causes of Microtubule Catastrophe and Aging. *Biophys. J.* 109:2574–2591. https://doi.org/10.1016/j.bpj.2015.10.048.

60. McIntosh, J. R., E. O'Toole, …, N. Gudimchuk. 2018. Microtubules grow by the addition of bent guanosine triphosphate tubulin to the tips of curved protofilaments. *J. Cell Biol.* 217:2691–2708. https://doi.org/10.1083/jcb.201802138.

61. Molodtsov, M. I., E. A. Ermakova, …, F. I. Ataullakhanov. 2005. A molecular-mechanical model of the microtubule. *Biophys. J.* 88:3167–3179. https://doi.org/10.1529/biophysj.104.051789.

62. Bollinger, J. A., and M. J. Stevens. 2019. Diverse balances of tubulin interactions and shape change drive and interrupt microtubule depolymerization. *Soft Matter.* 15:8137–8146. https://doi.org/10.1039/c9sm01323g.

63. Michaels, T. C., S. Feng, …, L. Mahadevan. 2020. Mechanics and kinetics of dynamic instability. *Elife.* 9:e54077. https://doi.org/10.7554/eLife.54077.

64. Flyvbjerg, H., T. E. Holy, and S. Leibler. 1996. Microtubule dynamics: Caps, catastrophes, and coupled hydrolysis. *Phys. Rev. E.* 54:5538–5560. https://www.ncbi.nlm.nih.gov/pubmed/9965740.

65. Margolin, G., I. V. Gregoretti, …, M. S. Alber. 2006. Analysis of a mesoscopic stochastic model of microtubule dynamic instability. *Phys. Rev. E - Stat. Nonlinear Soft Matter Phys.* 74:041920. https://doi.org/10.1103/PhysRevE.74.041920.

66. van Haren, J., and T. Wittmann. 2019. Microtubule Plus End Dynamics - Do We Know How Microtubules Grow?: Cells boost microtubule growth by promoting distinct structural transitions at growing microtubule ends. *Bioessays.* 41:e1800194. https://doi.org/10.1002/bies.201800194.

67. Reid, T. A., C. Coombes, …, M. K. Gardner. 2019. Structural state recognition facilitates tip tracking of EB1 at growing microtubule ends. *Elife.* 8:e48117. https://doi.org/10.7554/eLife.48117.

68. Duellberg, C., N. I. Cade, and T. Surrey. 2016. Microtubule aging probed by microfluidics-assisted tubulin washout. *Mol. Biol. Cell.* 27:3563–3573. https://doi.org/10.1091/mbc.E16-07-0548.

69. Odde, D. J., L. Cassimeris, and H. M. Buettner. 1995. Kinetics of microtubule catastrophe assessed by probabilistic analysis. *Biophys. J.* 69:796–802. https://doi.org/10.1016/S0006-3495(95)79953-2.

70. Gardner, M. K., M. Zanic, …, J. Howard. 2011. Depolymerizing kinesins Kip3 and MCAK shape cellular microtubule architecture by differential control of catastrophe. *Cell.* 147:1092–1103. https://doi.org/10.1016/j.cell.2011.10.037.

71. Kalisch, S. M., L. Laan, and M. Dogterom. 2011. Force generation by dynamic microtubules in vitro. *Methods Mol. Biol.* 777:147–165. https://doi.org/10.1007/978-1-61779-252-6_11.

72. Taberner, N., G. Weber, …, M. Dogterom. 2014. Reconstituting functional microtubule-barrier interactions. *Methods Cell Biol.* 120:69–90. https://doi.org/10.1016/B978-0-12-417136-7.00005-7.

73. Aher, A., M. Kok, …, A. Akhmanova. 2018. CLASP Suppresses Microtubule Catastrophes through a Single TOG Domain. *Dev. Cell.* 46:40–58.e8. https://doi.org/10.1016/j.devcel.2018.05.032.

74. Pham, H. T. M. 2004. PE-CVD Silicon Carbide - a structured material for surface micromachined devices. *Doctoral Thesis.* 4:49–73, uuid:91e396a8-5857-4e93-ba27-8a82d0d9f2b7 (Doctoral thesis).

75. Montenegro Gouveia, S., K. Leslie, …, A. Akhmanova. 2010. In vitro reconstitution of the functional interplay between MCAK and EB3 at microtubule plus ends. *Curr. Biol.* 20:1717–1722. https://doi.org/10.1016/j.cub.2010.08.020.

76. Bieling, P., L. Laan, …, T. Surrey. 2007. Reconstitution of a microtubule plus-end tracking system in vitro. *Nature.* 450:1100–1105. https://doi.org/10.1038/nature06386.

77. Guizar-Sicairos, M., S. T. Thurman, and J. R. Fienup. 2008. Efficient subpixel image registration algorithms. *Opt. Lett.* 33:156–158.

78. Schindelin, J., I. Arganda-Carreras, …, A. Cardona. 2012. Fiji: an open-source platform for biological-image analysis. *Nat. Methods.* 9:676–682. https://doi.org/10.1038/nmeth.2019.

79. Maurer, S. P., N. I. Cade, …, T. Surrey. 2014. EB1 accelerates two conformational transitions important for microtubule maturation and dynamics. *Curr. Biol.* 24:372–384. https://doi.org/10.1016/j.cub.2013.12.042.

80. Dhar, S., O. Seitz, …, L. C. Feldman. 2009. Chemical properties of oxidized silicon carbide surfaces upon etching in hydrofluoric acid. *J. Am. Chem. Soc.* 131:16808–16813. https://doi.org/10.1021/ja9053465.

81. Coletti, C., M. J. Jaroszeski, …, S. E. Saddow. 2007. Biocompatibility and wettability of crystalline SiC and Si surfaces. *Conf. Proc. IEEE*

Eng. Med. Biol. Soc. 2007:5850–5853. https://doi.org/10.1109/IEMBS.2007.4353678.

82. Kim, T., and L. M. Rice. 2019. Long-range, through-lattice coupling improves predictions of microtubule catastrophe. *Mol. Biol. Cell.* 30:1451–1462. https://doi.org/10.1091/mbc.E18-10-0641.
83. Antal, T., P. L. Krapivsky, …, B. Chakraborty. 2007. Dynamics of an idealized model of microtubule growth and catastrophe. *Phys. Rev. E - Stat. Nonlinear Soft Matter Phys.* 76:041907. https://doi.org/10.1103/PhysRevE.76.041907.
84. von Loeffelholz, O., N. A. Venables, …, C. A. Moores. 2017. Nucleotide- and Mal3-dependent changes in fission yeast microtubules suggest a structural plasticity view of dynamics. *Nat. Commun.* 8:2110. https://doi.org/10.1038/s41467-017-02241-5.
85. Roth, D., B. P. Fitton, …, A. Straube. 2018. Spatial positioning of EB family proteins at microtubule tips involves distinct nucleotide-dependent binding properties. *J. Cell Sci.* 132:jcs219550. https://doi.org/10.1242/jcs.219550.
86. Mahserejian, S. M., J. P. Scripture, …, H. V. Goodson. 2022. Quantification of microtubule stutters: dynamic instability behaviors that are strongly associated with catastrophe. *Mol. Biol. Cell.* 33:ar22. https://doi.org/10.1091/mbc.E20-06-0348.
87. Mohan, R., E. A. Katrukha, …, A. Akhmanova. 2013. End-binding proteins sensitize microtubules to the action of microtubule-targeting agents. *Proc. Natl. Acad. Sci. USA.* 110:8900–8905. https://doi.org/10.1073/pnas.1300395110.
88. Maurer, S. P., F. J. Fourniol, …, T. Surrey. 2012. EBs recognize a nucleotide-dependent structural cap at growing microtubule ends. *Cell.* 149:371–382. https://doi.org/10.1016/j.cell.2012.02.049.
89. Schwietert, F., L. Heydenreich, and J. Kierfeld. 2023. Dynamics and length distributions of microtubules with a multistep catastrophe mechanism. *New J. Phys.* 25:013017. https://doi.org/10.1088/1367-2630/acb07b.
90. Chretien, D., S. D. Fuller, and E. Karsenti. 1995. Structure of growing microtubule ends: two-dimensional sheets close into tubes at variable rates. *J. Cell Biol.* 129:1311–1328. https://doi.org/10.1083/jcb.129.5.1311.
91. Meadows, J. C., L. J. Messin, …, J. B. Millar. 2018. Opposing kinesin complexes queue at plus tips to ensure microtubule catastrophe at cell ends. *EMBO Rep.* 19:e46196. https://doi.org/10.15252/embr.201846196.
92. Sirajuddin, M., L. M. Rice, and R. D. Vale. 2014. Regulation of microtubule motors by tubulin isotypes and post-translational modifications. *Nat. Cell Biol.* 16:335–344. https://doi.org/10.1038/ncb2920.
93. Fees, C. P., and J. K. Moore. 2018. Regulation of microtubule dynamic instability by the carboxy-terminal tail of beta-tubulin. *Life Sci. Alliance.* 1:e201800054. https://doi.org/10.26508/lsa.201800054.
94. Farmer, V., G. Arpag, …, M. Zanic. 2021. XMAP215 promotes microtubule catastrophe by disrupting the growing microtubule end. *J. Cell Biol.* 220:e202012144. https://doi.org/10.1083/jcb.202012144.